Liner Implosion Experiments Driven by a Dynamic Screw Pinch

Paul C. Campbell,[1, a)] T. M. Jones,[1] J. M. Woolstrum,[1] N. M. Jordan,[1] P. F. Schmit,[2] A. L. Velikovich,[3] J. B. Greenly,[4] W. M. Potter,[4] E. S. Lavine,[4] B. R. Kusse,[4] D. A. Hammer,[4] and R. D. McBride[1]

[1)] *Nuclear Engineering and Radiological Sciences, University of Michigan, Ann Arbor, MI 48109, USA*

[2)] *Sandia National Laboratories, Albuquerque, NM 87185, USA*

[3)] *Plasma Physics Division, Naval Research Laboratory, Washington, DC 20375, USA*

[4)] *Laboratory of Plasma Studies, Cornell University, Ithaca, NY 14853, USA*

(Dated: 12 July 2021)

This paper expands upon recent experimental results [P. C. Campbell *et al.* Phys. Rev. Lett. **125**, 035001 (2020)], where thin-foil liner implosions were driven by a dynamic screw pinch (DSP) and found to have magneto-Rayleigh-Taylor instability (MRTI) amplitudes up to three times smaller than in implosions driven by a standard z-pinch (SZP). The expanded discussion presented herein includes: (1) a detailed comparison of the MRTI growth measured in experiment with that calculated from theory; (2) measurements of axial magnetic field injection into the liner interior prior to the implosion, as well as the subsequent compression of this field during the implosion; (3) an in-depth description of how the helical geometry of the DSP can result in earlier implosion and stagnation times relative to the SZP; and (4) particle-in-cell simulations showing different electron drift behavior in the anode-cathode gap of the DSP relative to the SZP, and how this difference may be related to the different current waveforms recorded during the experiments.

I. INTRODUCTION

One of the most commonly studied plasma compression techniques is the fast z-pinch implosion,[1,2] where an electrical current density $\mathbf{J} = J_z\,\hat{\mathbf{z}}$ flows along a conducting cylindrical shell and generates an azimuthal magnetic field $\mathbf{B} = B_\theta\,\hat{\boldsymbol{\theta}}$, resulting in a $\mathbf{J} \times \mathbf{B}$ force density (due to the Lorentz force) that accelerates the cylindrical shell radially inwards. We will refer to this configuration as the standard z-pinch (SZP). This platform is used to study material properties,[3,4] laboratory astrophysics,[5,6] radiation generation,[7,8] and magneto-inertial fusion concepts such as Magnetized Liner Inertial Fusion (MagLIF).[9–11] MagLIF is currently being studied on the 25-MA, 100-ns Z facility at Sandia National Laboratories, where a thick metal tube (or "liner") is imploded to compress preheated and premagnetized fusion fuel.[12,13]

In order to reach the extreme conditions needed for high energy density physics applications, the cylindrical implosion must remain sufficiently uniform. However, the fast z-pinch process is susceptible to magnetohydrodynamic (MHD) instabilities (MHDI), including the sausage instability, the kink instability, higher-order helical instabilities in general, and the magneto-Rayleigh-Taylor (MRT) instability (MRTI).[14–21] Instability modes where the wave vector $\mathbf{k}$ and the driving magnetic field $\mathbf{B}$ satisfy $\mathbf{k} \cdot \mathbf{B} = 0$ will be the fastest growing modes since they will not be affected by the stabilizing influence of magnetic tension. In the SZP case, this means that the fastest growing modes will be azimuthally symmetric (with an azimuthal mode number $m = 0$).

Several techniques have been employed to stabilize z-pinch implosions.[20,22–28] For initially solid-metal liners, many of the techniques have involved mitigating the effects of the electrothermal[29,30] and electrochoric[31] instabilities (ETI and ECI, respectively). These instabilities result in early-time, non-uniform material ablation/expansion away from the liner's outer surface, which is thought to seed MRTI growth later in time. To tamp the material expansion, dielectric coatings have been applied to the liner's outer surface.[29,30,32] Additionally, ETI and ECI are material dependent and have been combated through liner material choices—e.g., tantalum liners appear more stable than aluminum and titanium liners.[33]

Another instability control technique is the use of thick liner walls. Since MHDI growth is driven primarily at the liner's outer surface, MagLIF liners on the Z facility use thick liner walls to prevent MHDI feedthrough from perturbing the fusion fuel enclosed inside.[34,35] However, using such thick liners reduces the implosion velocity and thus reduces the achievable fusion yield.

An instability control method that does not rely on the use of thick liner walls, dielectric coatings, or specific material choices is the dynamic screw pinch (DSP). This technique was originally used to stabilize gas-puff z-pinch implosions in Refs. 36–38. For initially solid-metal liner implosions, this concept was proposed and studied numerically in Ref. 39, studied in simulation in Ref. 40, and studied in experiment in Ref. 41.

In contrast to the straight return-current structure of a SZP, the DSP is generated using a helical return-current structure (see Fig. 1). The helical return-current path results in a helical magnetic field, $\mathbf{B}(t) = B_\theta(t)\hat{\boldsymbol{\theta}} + B_z(t)\hat{\mathbf{z}}$, which drives the implosion. At the liner's outer surface, with a radius of $r_\ell(t)$, the two field components are given by $B_\theta(t) \approx \mu_0 I(t)/[2\pi r_\ell(t)]$ and $B_z(t) \approx \mu_0 n_c I(t)$, where n_c is the number of turns per unit length of the helical return-current structure. Note that the ratio $B_z(t)/B_\theta(t) \propto r_\ell(t)$ and the helical pitch angle of the magnetic field $\phi_B(t) = \arctan[B_z(t)/B_\theta(t)] =$

[a)] Author to whom correspondence should be addressed: pccamp@umich.edu

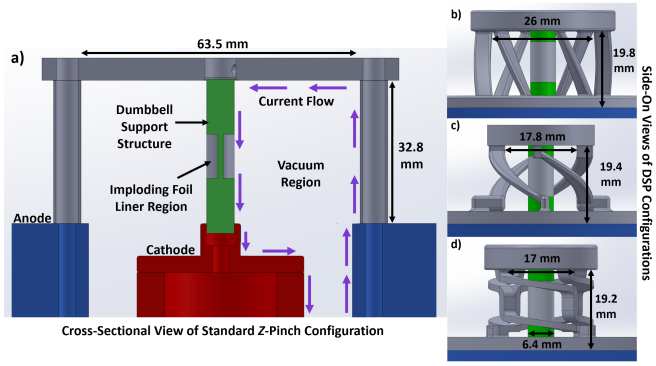

FIG. 1. CAD models of the return-current structures tested in these experiments. (a) The straight return-current structure of the SZP with an illustration of the power feed. (b) The low-field DSP return-current structure, predicted to have a peak axial field of 2 T. (c) The mid-field DSP return-current structure, predicted to have a peak axial field of 14 T. (d) The high-field DSP return-current structure, predicted to have a peak axial field of 20 T. Heights are measured from the top of the anode plate (blue) to the bottom of the return-current structure's lid. Diameters are measured from the inside edges of the return-current posts/twists. The imploding foil liner has an initial radius of 3.175 mm and a height of 10 mm. Reproduced with permission from Phys. Rev. Lett. **125**, 035001 (2020). Copyright 2020 American Physical Society.

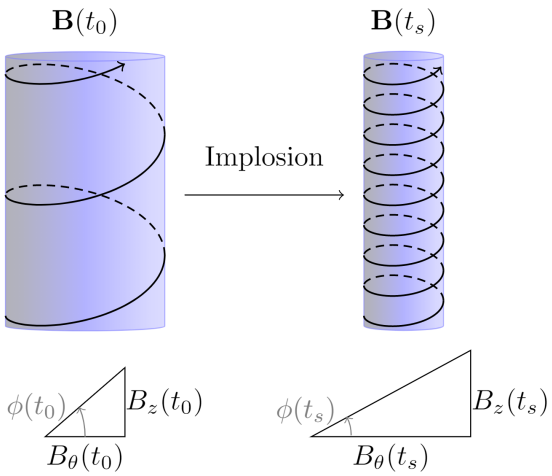

FIG. 2. An illustration of a DSP-driven liner implosion along with representations for how the magnetic field components will evolve as the liner implodes. The axial component is proportional to the driving load current, $I(t)$, throughout the implosion, while the azimuthal component is proportional to $I(t)/r_\ell(t)$, where $r_\ell(t)$ is the radius of the liner's outer surface. Thus, as $r_\ell(t)$ goes to zero, the magnetic field's pitch angle $\phi_B(t)$ goes to zero. Note that the field components being illustrated here are along the liner's outer surface, not the inner surface.

$\arctan[2\pi n_c r_\ell(t)]$ remain fixed until the liner starts to implode. As $r_\ell(t)$ decreases, $\phi_B(t)$ decreases, and $\mathbf{B}(t)$ approaches a pure azimuthal field (see Fig. 2).

As a DSP-driven liner implodes, the perturbation pitch angle that satisfies $\mathbf{k}\cdot\mathbf{B}=0$ changes continuously, since $\phi_B(t)$ changes continuously. By contrast, in a SZP-driven implosion, the magnetic field is purely azimuthal [$\mathbf{B}=B_\theta(t)\,\hat{\boldsymbol{\theta}}$], and thus $\phi_B=0$ throughout the implosion. In the SZP case, $\mathbf{k}\cdot\mathbf{B}=0$ is satisfied only for azimuthally symmetric modes with axially directed perturbation wave vectors (i.e., $m=0$, $\mathbf{k}=k_z\hat{\boldsymbol{z}}$).

The rotating $\phi_B(t)$ in the DSP case results in less cumulative instability growth relative to the SZP case. For example, in Ref. 39, linear perturbation theory was used to study single-mode instability growth in thick-shell liner implosions. The results suggested that by an implosion convergence ratio [$C_r\equiv r_\ell(0)/r_\ell(t)$] of 4–8, the cumulative exponential growth for a DSP-driven implosion could be 1 to 2 orders of magnitude less than that of a SZP-driven implosion for modes with final perturbation wavelength magnitudes of 200–400 μm.

It is important to note that the $B_z(t)\approx\mu_0 n_c I(t)$ described above for the DSP-driven system is distinctly different from the axial magnetic field that is pre-imposed in the standard MagLIF concept. In standard MagLIF, the pre-imposed axial field, $B_{z0}\approx$ 10–20 T, is applied by pulsing a pair of external Helmholtz-like coils over a long timescale (∼ms). The coils surround the entire load region, including both the liner target and the return-current structure (see Fig. 2 in Ref. 42, for example). Because of the long timescale, the pre-imposed axial field diffuses into all structures (including the metal liner and the metal electrodes) and permeates the entire experimental region prior to the start of the relatively fast liner implosion (∼100 ns). Because of the large size of the coils, the fully diffused field (just prior to the implosion) is approximately uniform throughout the load region; thus, since there is no significant magnetic pressure *gradient*, the background axial field does not contribute to driving the implosion. Once the background axial field has fully diffused into the load region, the Z machine is triggered to drive the implosion. Thus, we refer to standard MagLIF as a SZP-driven system in the presence of a background axial magnetic field.

During a standard MagLIF implosion, the pre-imposed axial field inside the liner (within the fuel region) is amplified to >1000 T via flux compression. That is, on the timescale of the implosion (∼100 ns), the pre-imposed axial field is trapped inside the liner and frozen into the preheated MagLIF fuel. The amplified field is needed to insulate the hot fuel from the cold liner wall and to trap charged fusion products (e.g., α particles and tritons) in the fuel for self-heating.[43]

In contrast with the axial field in SZP-driven MagLIF, the fast $B_z(t)\approx\mu_0 n_c I(t)$ in a DSP configuration contributes to driving the implosion and is nominally excluded from the liner interior (though there are exceptions to the flux exclusion—see Sec. III A in this paper as well as Refs. 40 and 44). It is also important to note that a DSP-driven configuration can accommodate

a Helmholtz-like coil system, thus a background B_{z0} can be applied in addition to the $B_z(t) \approx \mu_0 n_c I(t)$ generated by the DSP's helical return-current structure. In fact, a background B_{z0} was included in the DSP configurations explored in Ref. 39 (the original concept paper for DSP-driven MagLIF). However, we emphasize that the experiments presented in this paper and in Ref. 41 do not include a background B_{z0}.

In standard MagLIF, the pre-imposed axial field does not contribute to driving the implosion, but it does affect the development of MHDI. For example, in SZP-driven liner implosion experiments conducted on the Z facility with $B_{z0} \approx 10$ T, penetrating radiography revealed that helical instability modes developed with $m \approx 6$ and helical pitch angles of approximately 30° by the time the liner's inner surface had imploded to an inner-surface convergence ratio [$C_{r,\text{in}} \equiv r_{\text{in}}(0)/r_{\text{in}}(t)$] of approximately 7.[45] These experiments showed less instability feedthrough than experiments conducted without a background axial field, where only non-helical (azimuthally symmetric) instability modes were observed.[34,35] Similarly, helical modes were observed in SZP-driven thin-foil liner implosions in the presence of a background $B_{z0} \approx 0.5$–2 T on the 1-MA, 100-ns MAIZE facility at the University of Michigan.[46]

In the SZP-driven experiments of Refs. 45 and 46 (conducted with a pre-imposed B_{z0}), the pitch angle of the global magnetic field just outside the liner [i.e., the superposition of the pre-imposed B_{z0} and the implosion-driving $B_\theta(t)$] should rotate rapidly from 90° (just prior to the pulsed-power machine firing) to nearly 0° (when the pulsed-power machine reaches peak current). However, since nearly all of this rotation happens prior to the implosion (i.e., prior to liner acceleration and thus prior to MRTI growth), the pitch-angle rotation of the magnetic field is not expected to be a dominant stabilization mechanism (as it is expected to be in DSP-driven implosions). The reason for the enhanced stability (and the development of helical instability structures) in the experiments of Ref. 45 and 46 is still the subject of some debate, but it may involve magnetic shear,[20,22] flux compression of B_{z0} in the low-density plasma surrounding the liner,[47,48] a Hall instability in the low-density plasma surrounding the liner,[49] and/or field-aligned (force-free) currents.[50]

The results of Refs. 45 and 46 (SZP-driven with a pre-imposed B_{z0}) should not be confused with the results of Ref. 41 (DSP-driven without a pre-imposed B_{z0}). The reason for possible confusion is that both systems involve axial magnetic fields and both systems excite helical instability modes (e.g., see Sec. III B below). While there are likely overlapping physics issues pertaining to the development of MRTI in both systems, we emphasize that the two configurations are in fact distinctly different.

Beyond enhanced stability, the DSP also provides benefits in power coupling. For example, due to the additional magnetic drive pressure from the B_z component, a DSP-driven MagLIF implosion is expected to reach stagnation about 10 ns earlier than a standard MagLIF implosion, assuming the same current pulse is delivered to the load in both cases.[39] Alternatively, for the same implosion time, the DSP can drive a liner with a larger initial radius and thus impart more kinetic energy into the imploding shell.[38] An extended discussion on some of the subtler points of how the DSP configuration results in additional drive pressure is provided in Appendix A.

The remainder of this paper reviews and expands upon the DSP experiments presented in Ref. 41. It is organized as follows. In Sec. II, the experimental setup is reviewed with new details provided, such as the initial magnetic field pitch angles tested. In Sec. III A, we present new measurements of axial magnetic field injection into the liner interior prior to the implosion, as well as the subsequent compression of this field during the implosion. In Sec. III B, we review the stability results of Ref. 41 while also presenting new comparisons of the MRTI growth measured in experiment with that calculated using the analytic theory of Ref. 51. In Sec. III C, we present stagnation timing data for the SZP/DSP cases tested, along with attempts to calculate these data using simple thin-shell modeling. In Sec. III D, we present new particle-in-cell simulation results that show different electron drift behavior in the anode-cathode gap of the DSP relative to the SZP, which may be related to the different current waveforms recorded during the experiments of Ref. 41. In Sec. IV, we summarize this work and discuss opportunities for future DSP research.

II. EXPERIMENTAL SETUP

The DSP and SZP experiments presented in this paper and in Ref. 41 were conducted on the COBRA pulsed power facility at Cornell University. COBRA is a Marx-generator-based, low-impedance (0.5 Ω) driver used for high-energy-density plasma experiments.[52,53] In short-pulse mode, COBRA's load current rises to approximately 1 MA in 100 ns, while in long-pulse mode, the current rises to about 0.9 MA in 200 ns.

To study the physics of liner implosions on COBRA, thin-foil liners are used, since 1-MA, 100-ns machines lack the energy needed to implode massive, thick-walled MagLIF-like liners. For these experiments, 650-nm-thick aluminum foils were used, along with an initial liner radius of 3.175 mm.

An important parameter for characterizing the liner's susceptibility to MHDI feedthrough is the liner's initial aspect ratio, $A_{r0} \equiv r_{\ell 0}/\delta_0$, where $r_{\ell 0}$ is the initial radius of the liner's outer surface, and δ_0 is the liner's initial wall thickness. For our thin-foil liners, $A_{r0} \sim 6{,}000$. By contrast, the more robust MagLIF liners on the Z facility typically use $A_{r0} \approx 6$, where $r_{\ell 0} \approx 3$ mm, and $\delta_0 \approx 500$ μm. Thus, for MagLIF on Z, the wall thickness is greater than the electrical skin depth, $\delta_e \sim 100$ μm. This is not the case for our 650-nm-thick thin-foil liners on COBRA.

One may rightfully question how this large difference in A_{r0} could result in experiments that are relevant to MagLIF. The answer is that because $\delta_0 < \delta_e$, intense ohmic heating causes the thin-foil liner wall to expand rapidly to $\delta \sim$ 100–1000 μm well before the implosion starts.[54,55] This lowers the *effective* A_{r0} to 3–30. Additionally, MRTI growth is governed primarily by the acceleration history of the implosion,[14] thus our MagLIF-relevant implosion trajectories (roughly 3 mm in 100 ns) should result in MagLIF-relevant MRTI growth. Furthermore, we note that other thin-foil liner implosion experiments have already demonstrated relevancy to MRTI growth in MagLIF.[46,56]

The thin-foil liners used in our experiments are not nearly as robust as the freestanding liners used in MagLIF experiments on Z. Thin-foil liners are easily crinkled, resulting in larger seed perturbation amplitudes. Furthermore, the liners are not self-supporting. Thus, following Ref. 57, the liner loads were assembled by wrapping a rectangular foil onto a plastic dumbbell-shaped support structure (see Fig. 1). The dumbbell ends have the same diameter as the chosen liner diameter, while the connecting rod in the central portion of the support structure has as small of a diameter as possible to allow as much implosion convergence as possible. For our experiments, the central portion of the dumbbell (the on-axis support rod) had a radius of 0.65 mm, which allowed for a nominal thin-shell convergence ratio ($C_r \equiv r_{\ell 0}/r_{\ell f}$) of up to 4.9. However, the maximum convergence ratio observed in our experiments (for the liner's outer surface) was approximately 2. Finally, there is a thin seam where the rectangular foil, wrapped into a cylindrical shell, overlaps itself. This seam was positioned azimuthally to minimize interference with imaging diagnostics and instability measurements.

For these experiments, one straight return-current structure (SZP) and three different helical return-current structures (DSPs) were designed, simulated, fabricated, and tested (see Fig. 1). For the design, CST EM Studio,[58] a 3D electromagnetics analysis software package, was used. The goal was to keep the load inductance below 10 nH, as this is the inductance that COBRA was designed to drive. Despite their helicity, the DSP return-current structures had inductance values similar to that of the SZP return-current structure, because the SZP structure was both taller and wider than the DSP structures. The simulated inductances for these return-current structures were 8.32 nH for the SZP, 6.61 nH for the low-field DSP, 6.98 nH for the mid-field DSP, and 9.76 nH for the high-field DSP. The SZP return-current structure was machined out of 304 stainless steel, while the twisted DSP structures were 3D printed using a binder jetting process from a mixture of 316 stainless steel and bronze (60% steel, 40% bronze). Useful metrics for characterizing the helical strength of each SZP/DSP design tested on COBRA are provided in Table I.

Note that these experiments did *not* involve a pre-imposed/background axial magnetic field like that used in MagLIF—i.e., supplemental/external Helmholtz-like coils were *not* used in any of the SZP or DSP experiments reported herein.

TABLE I. Parameters to characterize the four return-current structures tested on COBRA, including the peak B_z generated, $B_{z,\text{peak}}$, the number of turns per unit length, n_c, the initial ratio of the magnetic field components at the liner's outer surface, $\beta_0 \equiv [B_z/B_\theta]_{r_\ell = r_{\ell 0}}$, the initial pitch angle of the driving magnetic field, $\phi_{B,0} \equiv \arctan[B_z/B_\theta]_{r_\ell = r_{\ell 0}}$, and the gain in magnetic pressure, $G_0 = (2\pi r_{\ell 0} n_c)^2 \cdot 100\%$, that the DSP provides when the liner is at its initial position, $r_{\ell 0}$. Note that $\beta = \beta_0$, $\phi_B = \phi_{B,0}$, and $G = G_0$ all remain constant until the liner starts to implode.

Pinch Type	$B_{z,\text{peak}}$ (T)	n_c (1/cm)	β_0	$\phi_{B,0}$	G_0
SZP	0	0	0	0°	0%
Low-Field DSP	2	0.014	0.028	1.6°	0.08%
Mid-Field DSP	14	0.094	0.19	10.6°	3.5%
High-Field DSP	20	0.138	0.28	15.4°	7.6%

III. EXPERIMENTAL RESULTS

A. Axial magnetic field injection and compression

The axial magnetic fields generated by the return-current structures were measured with a micro B-dot probe[59] placed 3 mm radially outward from the liner surface. The uncertainty in the probe measurements is ±10%.[60] The drive current was measured using a Rogowski coil in COBRA's power feed. Examples of outer axial field and current measurements are presented in Fig. 2 of Ref. 41.

The axial field measurements agree reasonably well with the values predicted by CST design simulations. The low-field experiments had measured peak values of 3.5±2.1 T, while the mid-field experiments had measured peak values of 11.5 ± 5.3 T. The probe failed on the only high-field shot. Note that, in Fig. 2 of Ref. 41, the $B_z(t)$ waveform matches the drive current waveform very well during the rising edge of the pulse. After peak current, however, the micro B-dot probe appears to short out (as is indicated by this time-integrated signal not returning to zero). This behavior was consistent across other shots as well. During post-shot inspections, it was discovered that the dielectric insulator that covers the probe was compromised, which is likely related to the probe failures after peak current.

The simulation results presented in Refs. 40 and 44 suggest that the DSP configuration could be used to inject B_z into the MagLIF fuel, potentially removing the need for external B_z coils. Thus, micro B-dot probes were placed inside the liners on COBRA to measure B_z injection and compression (see Figures 3 and 4). The probes were housed within the on-axis support rod to minimize interference with the liner implosion. The on-

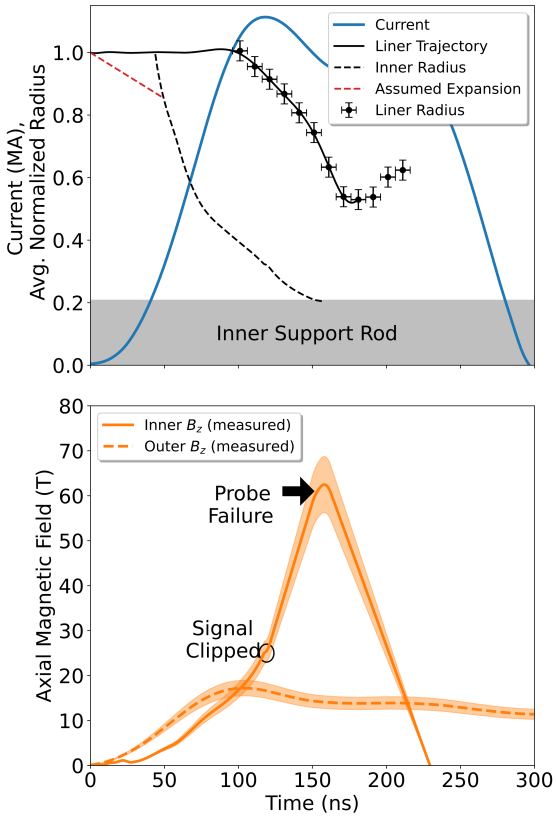

FIG. 3. Experimental data from shot 5396, which used the mid-field DSP configuration. (Top) Measured radius of the liner's outer surface (black filled circles), calculated radius of the liner's inner surface (dashed line), a fit to the liner's outer surface trajectories (black line), and drive current (blue line). The radius of the inner support rod is also shown. (Bottom) Plots of the measured axial magnetic field inside and outside the liner (orange lines; the orange shading represents the measurement uncertainty). Note that the signal for the inner axial field measurement clipped on the oscilloscope prior to probe failure, so the measured peak value is lower than it should be. Further note that failure in these probes is indicated consistently (across many different experiments and many different experimental platforms) by the probe voltage swinging strongly negative.

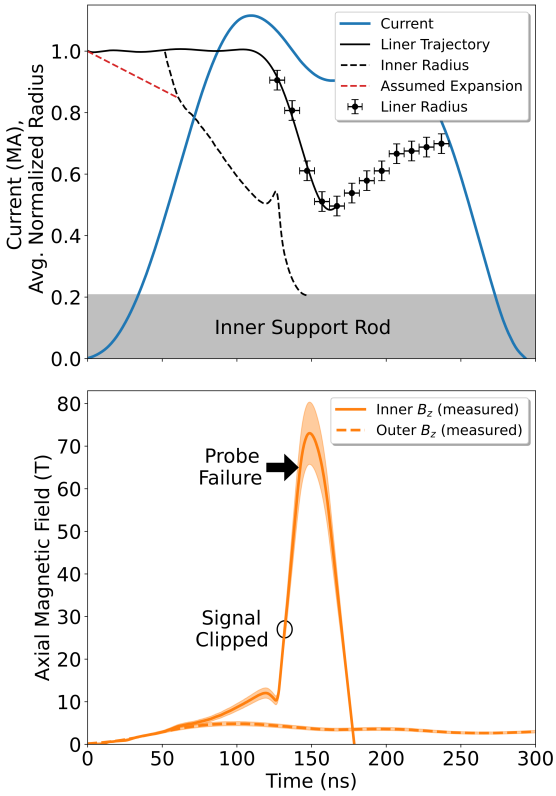

FIG. 4. Experimental data from shot 5403, which used the low-field DSP configuration. (Top) Measured radius of the liner's outer surface (black filled circles), calculated radius of the liner's inner surface (dashed line), a fit to the liner's outer surface trajectories (black line), and drive current (blue line). The radius of the inner support rod is also shown. (Bottom) Plots of the measured axial magnetic field inside and outside the liner (orange lines; the orange shading represents the measurement uncertainty). Note that the signal for the inner axial field measurement clipped on the oscilloscope prior to probe failure, so the measured peak value is lower than it should be.

axis B-dot probe configuration was fielded on several low-field and mid-field shots, along with the one high-field shot. The measurements had large shot-to-shot variations (even for the same DSP case being tested multiple times). The large variations may be explained by the somewhat random timing of when the probes failed. In some cases, probe failure occurred when the liner stagnated upon the on-axis support rod. In other cases, the B-dot probes failed before stagnation. Additionally, in some cases, the signal was clipped on the oscilloscope. For the probes that failed before stagnation and/or the signals that clipped, the full flux compression was not measured.

These measurements can be explained and modeled as follows. Early in the current pulse, the electrical skin depth is greater than the foil thickness, and thus the B_z component of the drive field can penetrate the liner interior rapidly during this period. Note that the B_θ component can also penetrate during this period if there is an axial current path available within the liner interior. If there is no internal path available, then B_θ will be confined to the liner wall and radially outside of the liner wall. By contrast, the B_z component does not require an internal current path for B_z to fill the liner interior. The B_z penetration continues even as the foil thickness increases due to ohmic heating, melting, and vaporization, since the unionized liquid-vapor state is highly resistive. Once the liquid-vapor state ionizes into a highly conductive plasma, both components of the external drive field become largely excluded from the liner's interior. However, whatever B_z flux penetrated the liner's inte-

rior prior to plasma formation is now trapped within the liner and can be flux compressed by the subsequent implosion of the liner. Note that these initial processes (up to and including plasma formation) occur early in the experiment, when the drive current is still low and the liner is still at its initial radius, $r_{\ell 0}$. Also note that during this period of B_z injection, the current density in the liner wall will be predominantly axial. Upon plasma formation, the current density will become helical, acquiring a stronger azimuthal component to exclude B_z from the liner's interior.

Once the liner has become a highly conductive plasma shell, the trapped B_z flux will be compressed by the inward motion of the liner's inner surface, with a radial trajectory denoted by $r_{\rm in}(t)$. This trajectory can be estimated using our on-axis $B_z(t)$ measurements and assuming perfect flux conservation throughout the implosion. To do this, we assume that the probe fails when the liner's inner surface hits the on-axis support rod that houses the probe. The radius of the on-axis support rod is $r_{\rm rod} = 0.65$ mm. The B_z value measured just prior to probe failure is the peak value, $B_{z,\rm peak}$. Thus, the axial flux at this point is $\Phi_z = \pi r_{\rm rod}^2 \cdot B_{z,\rm peak}$. With Φ_z conserved throughout the implosion, we obtain $r_{\rm in}(t)$ from our $B_z(t)$ waveforms using $\Phi_z = \pi r_{\rm in}^2(t) \cdot B_z(t)$.

In Figs. 3 and 4, the calculated $r_{\rm in}(t)$ trajectories are presented. Moving backwards in time from the point of probe failure, the $r_{\rm in}(t)$ curve approaches the liner's outer surface radius, $r_\ell(t)$. At some point during this approach, which happens rapidly near 50 ns, the shell thickness, $\delta(t) = r_\ell(t) - r_{\rm in}(t)$, becomes too thin to isolate the interior B_z field from the exterior B_z field. To estimate the shell thickness where this transition occurs, we used the diffusion time[61] $\tau_d(t) = \delta^2(t)\mu_0/\rho_e$, where ρ_e is the material's electrical resistivity. To evaluate ρ_e, we used a SESAME[62] conductivity table for aluminum. The SESAME table uses the quantum Lee-More-Desjarlais (QLMD) conductivity model, generated by tuning the wide-ranging Lee-More-Desjarlais algorithms[63] to quantum molecular dynamics/Kubo-Greenwood calculations of the conductivity.[64] This table, and thus ρ_e, depends on temperature and density. We obtained reasonable estimates of the temperature and density from previous thin-foil simulations.[49,55] With $\tau_d(t)$ evaluated at each point along the trajectory $r_{\rm in}(t)$, we then found the point where $\tau_d(t)$ becomes equal to the rise time of the driving current pulse, $\tau_r = 100$ ns. The time when this condition is met is denoted as t^*. In general, $t^* \approx 50$ ns. For $t > t^*$, $\delta(t)$ is thick enough for $\tau_d > \tau_r$, and thus the internal and external fields are isolated from one another and flux compression is possible. For $t < t^*$, $\delta(t)$ is thin enough for $\tau_d < \tau_r$, and thus the external drive field can penetrate the liner interior. Following this procedure, we found that $\delta^* \equiv \delta(t^*) \approx 500 \pm 100$ μm. In Figs. 3 and 4, we allowed $\delta(t)$ to grow linearly from $\delta_0 = 650$ nm at $t = 0$ to $\delta^* = 500$ μm at $t = t^*$. Beyond $t = t^*$, $r_{\rm in}(t)$ follows the trajectory determined from flux conservation.

Note that for $t > t^*$, the magnetic Reynolds number is estimated to be in the range of 1–10. Also note that since the signals from the inner B-dot probes clipped on the oscilloscope, Figs. 3 and 4 provide upper bounds on the liner shell thickness, $\delta(t) = r_\ell(t) - r_{\rm in}(t)$, and lower bounds on the liner's inner surface implosion velocity. That is, if the full signals had been measured (no clipping), then larger $B_{z,\rm peak}$ and Φ_z values would have been obtained. In Figs. 3 and 4, this would shift the points where the dashed black lines touch the solid black lines to later times, resulting in a thinner $\delta(t)$ up until the time of probe failure (when the dashed black lines touch the inner support rods). In Figs. 3 and 4, the points where the dashed black lines touch the inner support rods are not affected by clipping, because these points are fixed by the probe failure times and the known radius of the rods ($r_{\rm rod} = 0.65$ mm).

The inner surface trajectories illustrated in Figs. 3 and 4 could be due to low-density "precursor" plasma being ablated from the liner's inner surface and then being advected towards the on-axis B-dot probe ahead of the bulk liner motion. Note that with the liner's interior volume pre-filled with low-density gas (or ablated/advected plasma), subsequent bulk liner motion (even very small motion) can drive shockwaves through the low-density gas/plasma.[65] Shockwaves would further complicate our flux compression analysis, but they may also help to explain some subtleties in the data. For example, referring to the inner $B_z(t)$ signal shown in Fig. 4, a compressional wave passing through the system (in very low-density plasma), reflecting off the support rod, and subsequently being impacted by an incoming shockwave may explain the dip and subsequent rapid rise in the signal at $t \approx 130$ ns. Also note that a low-density precursor plasma would be more strongly affected by the back pressure due to the injected B_z field. Based on the small amount of flux assumed to be injected early in time and the limited implosion convergence provide by the on-axis support rod, the back pressure due to the injected $B_z(t)$ is not expected to significantly impact the implosion trajectories. However, the system is complex, and our measurements do not tell us the the field profile within the ablated plasma layer. Furthermore, we see from the outer surface trajectories in Figs. 3 and 4 that the implosions occur at different rates, suggesting that back pressure may indeed be at play. The above phenomena could be investigated in the future with end-on laser probing, penetrating side-on radiography (perhaps using X-pinches), and supporting MHD simulations. For now, the analysis presented here shows that, at least in principle, the measured $B_z(t)$ signals could have been generated by flux injection followed by flux compression.

B. Instability evolution and comparison with theory

To image the liner implosion dynamics and instability evolution, visible-light self-emission from the plasma was imaged using a fast 12-frame camera (see Fig. 5),

and extreme ultraviolet (XUV) self-emission light was imaged using two 4-frame cameras (see Fig. 6). The recorded images reveal the profound effects that the DSP had on the instability evolution. For example, helical modes were present in the DSP cases, while azimuthally symmetric modes were present in the SZP case (note that the helical modes are more easily seen in the XUV images). These observations are reminiscent of the helical striations observed previously on the surfaces of *non*-imploding foil-liner experiments with twisted return-current structures.[66]

As described in Ref. 41, the pitch angles of the imploding helical structures should evolve according to $\phi_{\rm plasma}(t) \approx \arctan\{p/[2\pi r_\ell(t)]\} \approx m/[k_z r_\ell(t)]$, where p is the helical pitch.[21,45,46] Importantly, p and m/k_z are preserved as these helical structures implode, since axial outflows are not permitted. This allows us to trace $\phi_{\rm plasma}(t)$ back to the time when the liner first began to implode. This initial plasma pitch angle, $\phi_{\rm plasma,0}$, can then be compared to the initial pitch angle of the driving magnetic field, $\phi_{B,0} = \arctan[B_z/B_\theta]_{r=r_{\ell 0}}$, which should have been constant up until the time when the liner started to implode. For example, in the XUV image of Fig. 6(b), $m/k_z = 23 \pm 8$ degree-mm, which traces back to $\phi_{\rm plasma,0} = 7 \pm 3°$, while $\phi_{B,0} = 6 \pm 1°$. These initial pitch angles are nearly equal (within uncertainties), implying that the observed $\phi_{\rm plasma}(t)$ is set by $\phi_{B,0}$. The seeding mechanism may involve the excitation of ETI and ECI at an angle consistent with $\phi_{B,0}$. Note that in the analysis of the high-field shot, we used calculated axial field values rather than measured field values due to the B-dot probe failure on the high-field shot.

From the analysis above, we see that $\phi_{\rm plasma}(t)$ increases throughout the implosion, while $\phi_B(t)$ decreases throughout the implosion (this is represented quantitatively in Fig. 7). This counterrotation implies that $\mathbf{k} \cdot \mathbf{B} \neq 0$ for the dominant helical structures observed in the DSP cases, which should imply enhanced stability for the DSP cases. From Fig. 7, we see that the high-field DSP case should be the most stable of the configurations tested. By contrast, there is no rotation of ϕ_B or $\phi_{\rm plasma}$ in the SZP case.

In Ref. 41, the visible imaging data were analyzed to extract the instability amplitude as a function of the liner's normalized distance moved, $\hat{d} \equiv 1 - r_\ell(t)/r_{\ell 0}$ (see Fig. 4 in Ref. 41). The results showed that the instability amplitudes for the mid-field and high-field DSP cases were smaller than in the SZP case by factors of about 2 and 3, respectively, at $\hat{d} = 0.5$ ($C_r = 2$). Specifically, at $\hat{d} = 0.5$ ($C_r = 2$), the MRTI amplitudes for the SZP case and for the 14-T and 20-T DSP cases were, respectively, 1.1±0.3 mm, 0.7±0.2 mm, and 0.3±0.1 mm.

The instability amplitudes presented in Fig. 4 of Ref. 41 were found by tracking the plasma-vacuum interface and taking the difference between the peaks and troughs along the left and right edges of the imploding plasma. However, this technique is only able to view the full depth of the troughs in the case of azimuthally symmetric ($m = 0$) instability structures (i.e., the SZP case). For the DSP cases, the helical pitch of the instability structures causes the peaks (spikes) to partially obscure the camera's view of the minimum radius in the troughs (bubbles). This then causes the instability amplitudes to appear smaller than their true values by some unknown factor.

To investigate the degree to which the helical viewing obstructions could be affecting the amplitude measurements, we constructed a geometrical model of the implosion for each DSP case. The perturbations were assumed to be cycloidal (i.e., sharp cusps[67,68]) to mimic the bubble-spike structure of the nonlinear instability development observed in the experiments. The perturbations also followed our assumed cascade through m and k_z space as the liner imploded (this cascade is discussed below). At each point in the implosion, a scale factor was determined between the true instability amplitude and the apparent instability amplitude (both amplitudes being well known in the geometrical model). This scale factor was then applied to the experiment data to obtain instability amplitudes that have been corrected for the assumed viewing obstruction. The results of this analysis are presented in Fig. 8. We see that the effect is fairly minimal; however, we caution that nonlinear instability structures are rarely pure cycloids. In future experiments, penetrating radiography will be attempted to eliminate this uncertainty.

To compare the measured instability growth with theory, we used the finite-thickness cylindrical shell model of Velikovich and Schmit (V&S).[51] This model is based on linear perturbation analysis and includes Bell-Plesset effects. In our experiments, we were not able to directly measure the position of the liner's inner surface, only the outer surface was imaged, so the in-flight shell thickness of the imploding liners is not known. However, based on the results of Refs. 54 and 55 (as well as on the flux compression results presented in Sec. III A), the thickness is likely in the range of 100–1000 μm.

In Fig. 9, the cumulative instability amplitude growth, Γ (the number of e-foldings), is plotted for the four experimental cases tested. The assumed liner thickness was 250 μm. These contour plots cover a large range of azimuthal mode numbers, m, and axial wave numbers, k_z, and they are computed up to $\hat{d} \approx 0.5$, which is the maximum value of $\hat{d}$ observed in the experiments. These plots are similar to those presented in Ref. 39. They illustrate the relative stabilization of $m = 0$ modes in the higher-field DSP cases (relative to the SZP case). They also illustrate the relative excitation of helical modes (with $m < 0$ and $k_z > 0$) in the higher-field DSP cases (relative to the SZP case). Importantly, though, the most rapidly growing modes in the DSP cases are more stable than the most rapidly growing modes in the SZP case.

The contour plots in Fig. 9 are useful for analyzing the cumulative single-mode growth from linear perturbation theory (i.e., for a single value of m and a single value of k_z, which are held constant over the entire implosion).

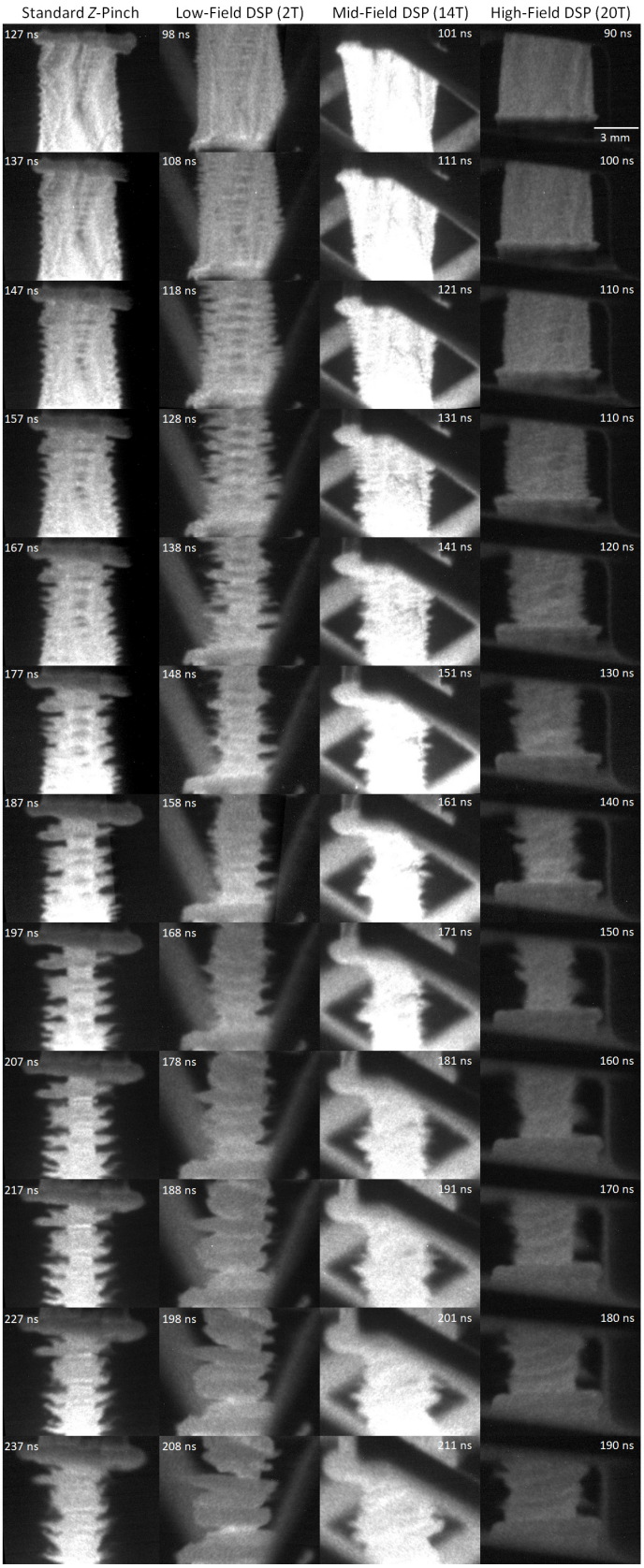

FIG. 5. Sample visible-light self-emission images showing the liner implosion dynamics from each of the experimental cases tested. Note that these images have not been contrast enhanced, but the low-field and high-field cases used an additional neutral density filter (ND=0.6) to avoid saturating the camera. This was done because the images recorded for the mid-field DSP case were significantly brighter than for the SZP case.

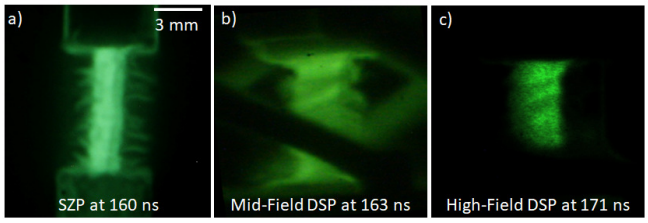

FIG. 6. Contrast enhanced XUV images taken near the time of stagnation for three of the experimental cases tested. (a) The SZP case. (b) The mid-field DSP case. (c) The high-field DSP case.

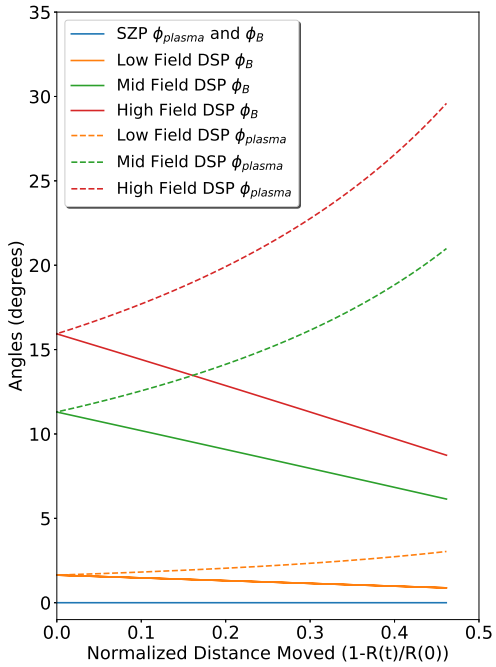

FIG. 7. Plots of the counterrotating pitch angles $\phi_B(t)$ and $\phi_{\rm plasma}(t)$ for each of the DSP cases tested. Note that there is no rotation for the SZP case.

However, in our experiments, we observed that the dominant instability structure cascaded from larger values of $|m|$ and k_z to smaller values of $|m|$ and k_z throughout the implosion. This inverse cascade is the result of nonlinear MRTI growth and mode merging events.

To account for the inverse cascade, we used the thick-shell V&S model to calculate the instability growth for a dominant perturbation structure that evolves according to our experimentally observed dominant perturbation structure—i.e., a perturbation structure with a rotating $\phi_{\rm plasma}(t)$ and a growing dominant wavelength. This perturbation was driven by the experimental magnetic field, with a pitch angle that rotates according to $\phi_B(t)$. For our wavelength evolution, we used $\lambda(\hat{d}) = [(\lambda_f - \lambda_i)/(\hat{d}_f - \hat{d}_i)]\hat{d} + \lambda_i$. This linear dependence assumption is based on the observations made in Ref. 34.

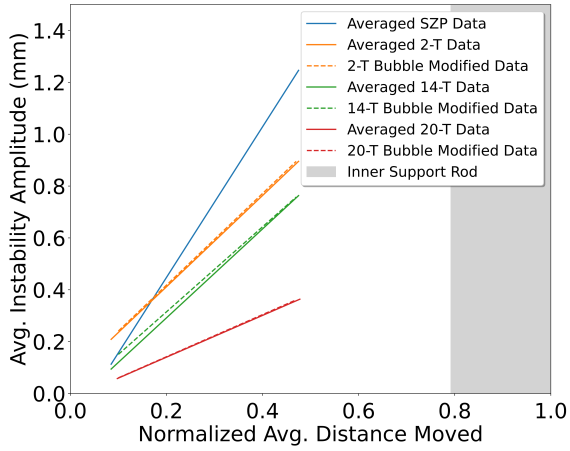

FIG. 8. Average instability amplitude as a function of the normalized distance moved, $\hat{d} = 1 - r_\ell(t)/r_{\ell 0}$, for the all experimental cases. This plot shows the degree to which the DSP measurements could be affected by the helical viewing obstructions described in the text. The average of the SZP cases would not be modified and are plotted for reference. This effect is a minor correction to all DSP cases, in the case of cusp like instability structures.

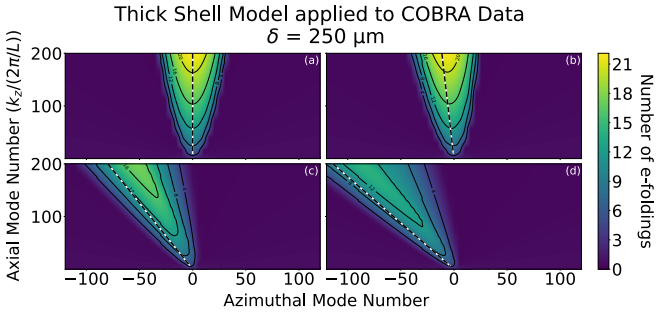

FIG. 9. Contour plots of the cumulative instability growth, Γ (number of e-foldings), for the four experimental cases tested, assuming a liner shell thickness of 250 μm. The e-foldings are calculated the using thick-shell model of Velikovich and Schmit[51] across a wide range of azimuthal mode numbers, m, and normalized axial wave numbers, $\hat{k} = k_z/(2\pi/L)$, where L is the axial length of the liner (1 cm). (a) The SZP case. (b) The low-field DSP case. (c) The mid-field DSP case. (d) The high-field DSP case. In these contour plots, each point represents an entire implosion simulation, with m and k_z held constant for the entire simulation. By contrast, the overlaid white and black dashed lines show the m and k_z values used in the inverse cascade model, which was used to generate Fig. 11. In the cascade model, m and k_z evolve along these dashed lines throughout the implosion simulation, as a function of $\hat{d}$, to mimic nonlinear MHDI evolution and mode merger events. The direction along these dashed lines is from higher $|m|$ and k_z values at $\hat{d} = 0$ to lower $|m|$ and k_z values as $\hat{d}$ approaches 1. Throughout the evolution, $m/k_z = \text{constant} = -r_{\ell 0} \tan \phi_{B,0}$. This cascade model is described in detail in the text. The overlaid dashed lines are presented only to illustrate the m and k_z values used in the cascade model; they are not directly related to the underlying contour plots.

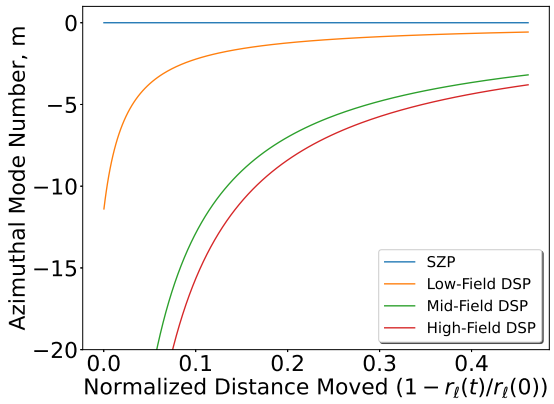

FIG. 10. A plot illustrating the evolution of the azimuthal mode number m as a function of $\hat{d}$ for all experimental cases.

We set the final wavelength values λ_f to those obtained from our imaging data: 1.0 mm, 1.0 mm, 1.25 mm, and 1.5 mm for the SZP, the low-field DSP, the mid-field DSP, and the high-field DSP, respectively. Since we do not know the initial perturbation wavelength λ_i, we used the smallest wavelength observed to maintain a dominant (coherent) perturbation structure. This value was found to be approximately 50 μm in Ref. 18.

From $\lambda(\hat{d})$ and $\phi_{\text{plasma}}(\hat{d})$, we obtained $\lambda_z(\hat{d}) = \lambda/\cos\phi_{\text{plasma}}$ and $k_z(\hat{d}) = 2\pi/\lambda_z$. The azimuthal mode numbers were determined from $m(\hat{d}) = -k_z r_{\ell 0}\tan\phi_{B,0}$, since the helical pitch p (and thus m/k_z) is preserved throughout the implosion (see Fig. 10). For the high-field DSP case, this results in an initial azimuthal mode number of $m \approx -113$ (in our experiments, the largest $|m|$ observed was in the mid-single digits, but this was due to diagnostic limitations and the much later time periods imaged in the experiments).

With $m(\hat{d})$ and $k_z(\hat{d})$ constructed, we must still set an initial perturbation amplitude, which is unknown. However, since we are only interested in the *relative* stability between the various SZP/DSP cases, we can simply choose whatever initial amplitude results in a match between theory and experiment for the SZP case at maximum convergence ($C_r = 2$, $\hat{d} = 0.5$) and then apply this same initial amplitude to all of the DSP cases. Doing this, we obtain the results presented in Fig. 11.

In Fig. 11(a), at $\hat{d} = 0.5$, the resulting amplitudes for the SZP case and for the 2-T, 14-T, and 20-T DSP cases are, respectively, 1.27 mm (by construction), 1.27 mm (i.e., no significant stabilization), 0.60 mm, and 0.34 mm. These amplitudes agree reasonably well with the amplitudes presented in Fig. 4 of Ref. 41. However, it is important to note that these amplitudes depend on the λ_{zf} values chosen and on the shell thickness chosen (for which we chose 250 μm in Fig. 11(a), based on the exploding thin-foil studies presented in Refs. 54 and 55). The model's sensitivities to the chosen values of λ_{zf} and shell thickness are illustrated by comparing Figs. 11(a)–11(d). Note that a wide range of shell thicknesses were considered (100–1000 μm) along with a modest range of final axial wavelengths (1–1.5 mm).

In Figs. 11(a) and 11(c), we used a shell thickness of 250 μm based on the exploding thin-foil studies presented in Refs. 54 and 55. By contrast, in Figs. 11(b) and 11(d), we used the upper limit shell thickness of 1000 μm. Note that the relative stabilizations obtained with the DSP cases increases as the shell thickness increases.

In Figs. 11(a) and 11(b), we used our imaging data taken at $\hat{d} = 0.5$ to set the final axial wavelengths (λ_{zf}) to 1 mm, 1 mm, 1.25 mm, and 1.5 mm for the SZP, the 2-T DSP, the 14-T DSP, and the 20-T DSP, respectively. By contrast, in Figs. 11(c) and 11(d), we set all final wavelength magnitudes to the same value ($\lambda_f = 1$ mm) so that $\lambda(\hat{d})$ would evolve exactly the same in each SZP/DSP case.

In comparing Fig. 11(a) with Fig. 11(c), it may appear that the relative stabilization obtained with the DSP has less to do with the counter rotating $\phi_B(t)$ and $\phi_{\text{plasma}}(t)$ and more to do with the fact that the higher-field DSP cases resulted in larger λ_f. This suggestion is further supported by the fact that results very similar to the ones shown in Fig. 11(a) can be obtained using the very simple MRTI growth rate formula: $\gamma = \sqrt{kg}$, where m and $\phi_B(t)$ have no effect, and where the degree of relative stabilization is determined solely by the values chosen for $\lambda_f = 2\pi/k_f$. If it holds true that the relative stabilization obtained in the experiments is due to the higher-field DSPs driving a cascade to larger λ_f, then this would be an interesting discovery. However, it is presently unclear as to why the DSP cases would drive the cascade to larger final wavelengths. Additionally, the relative stabilization obtained in the experiments may still be explained by the counter rotating $\phi_B(t)$ and $\phi_{\text{plasma}}(t)$ if the ohmically expanded shell thickness is large. For example, in Fig. 11(d), the use of a very thick shell (1000 μm) resulted in relative stabilizations that matched the experimental stabilizations reasonably well, even though the same λ_f values were used across all the SZP/DSP cases. In this scenario, all of the SZP/DSP cases would follow the exact same $\lambda(\hat{d})$ progression, and thus using the simple MRTI growth rate $\gamma = \sqrt{kg}$ would result in no relative stabilization, which is clearly not the case in the experiments.

To resolve whether the relative stabilization obtained in the experiments is due to the DSP cases driving the inverse cascade to larger final wavelengths or due to the counter-rotating $\phi_B(t)$ and $\phi_{\text{plasma}}(t)$ (or some combination of both), a good measurement of the ohmically expanded liner shell thickness is needed (perhaps from penetrating X-pinch radiography). Additionally, for the analyses presented in this paper, we have used a linear perturbation theory to describe a fundamentally nonlinear process (i.e., a wavelength cascade due to mode merger events). To model these nonlinear experiments more appropriately, 3D MHD simulations like those presented in Ref. 40 should be used. For example, this would

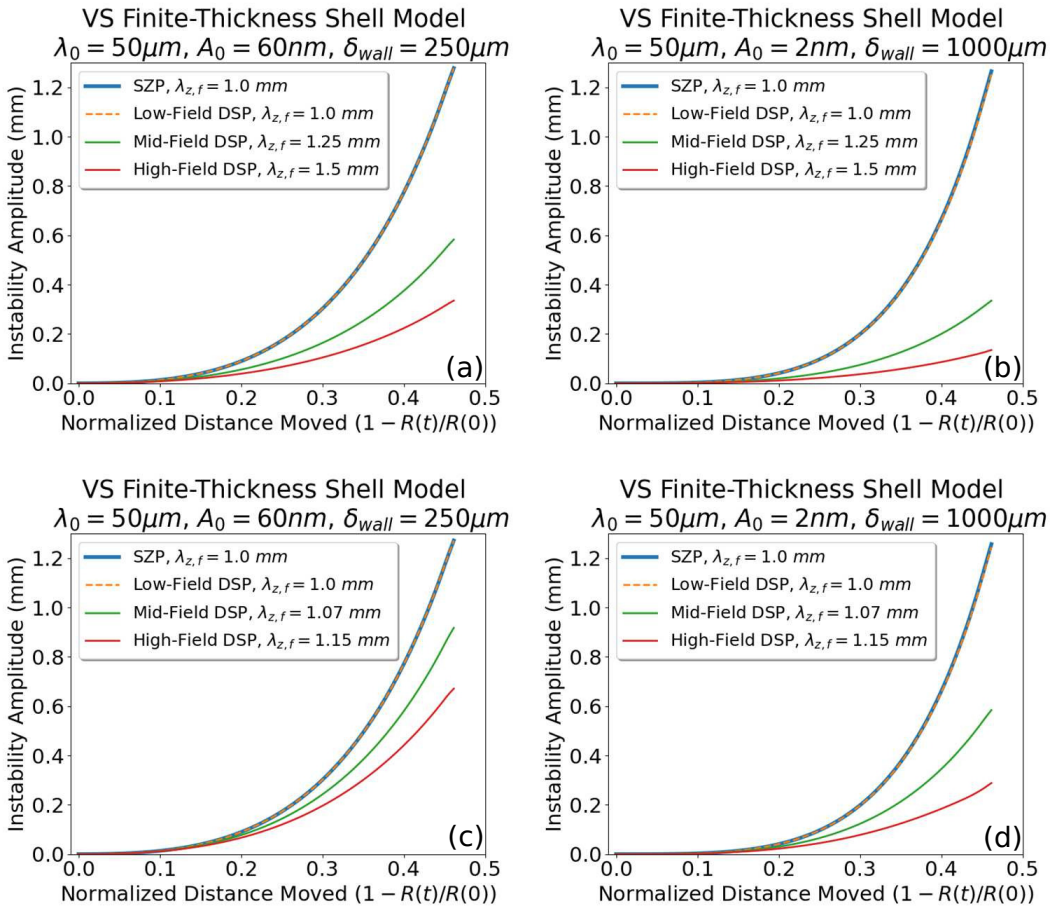

FIG. 11. Plots of the relative instability amplitude growth of a dominant perturbation structure with a pitch angle that rotates according to our experimentally observed $\phi_{\rm plasma}(t)$. These plots were generated using the thick-shell Velikovich and Schmit theory,[51] assuming a liner thickness of 250 μm (a,c) or 1000 μm (b,d). In applying the instability growth model, the initial perturbation wavelengths were all set to 50 μm, the initial perturbation amplitudes were set to either 60 nm (a,c) or 2 nm (b,d), and final axial wavelengths were set to either individually measured values for each SZP/DSP case (a,b) or to the same final wavelength value ($\lambda_f = 1$ mm) across all SZP/DSP cases (c,d). Note that the different λ_{zf} values for each SZP/DSP case in (c,d) are due solely to the geometrical projection $\lambda_{zf} = \lambda_f / \cos\phi_{\rm plasma}$, where only $\phi_{\rm plasma}$ is different in each SZP/DSP case; in (a,b), both λ_f and $\phi_{\rm plasma}$ are different in each SZP/DSP case. The case shown in (a) likely represents the best overall match to our experiments.

allow us to investigate whether the corrective term to the growth rate, proportional to $\mathbf{k} \cdot \mathbf{B}$, explains the cascade to larger λ_f values in the higher-field DSP cases. Such investigations will be pursued in the future.

C. Power coupling

In Ref. 41, it was noted that the DSP cases often stagnated 10–40 ns earlier than the SZP cases when considering only the short-pulse experiments (see the implosion trajectories presented in Fig. 2 of Ref. 41, for example). To provide further examples, here in Fig. 12, we have plotted the stagnation times collected from several short-pulse SZP and DSP experiments, along with the stagnation times predicted from simple thin-shell modeling.

For the thin-shell modeling in Fig. 12(a), 100% of the measured load current was assumed to flow along the liner's outer surface at $r = r_\ell(t)$. The modeling that considered only the drive pressure due to $B_\theta(t)$ (triangles) indicates that shot-to-shot variation in current delivery alone (∼10%) accounts for only 5–10 ns of variation in stagnation times across the SZP/DSP cases. When we include the drive pressures due to both $B_\theta(t)$ and $B_z(t)$ (squares), we find that the differences in stagnation times across the SZP/DSP cases does not increase by more than 5 ns. Also, when compared to the experiments, the modeled stagnation times for all of the SZP/DSP cases are too early by ∼70 ns. This large discrepancy could be an indication that substantially less current was delivered to the liner than was measured in the experiments (∼50% less, which we have little reason to suspect), or it could be an

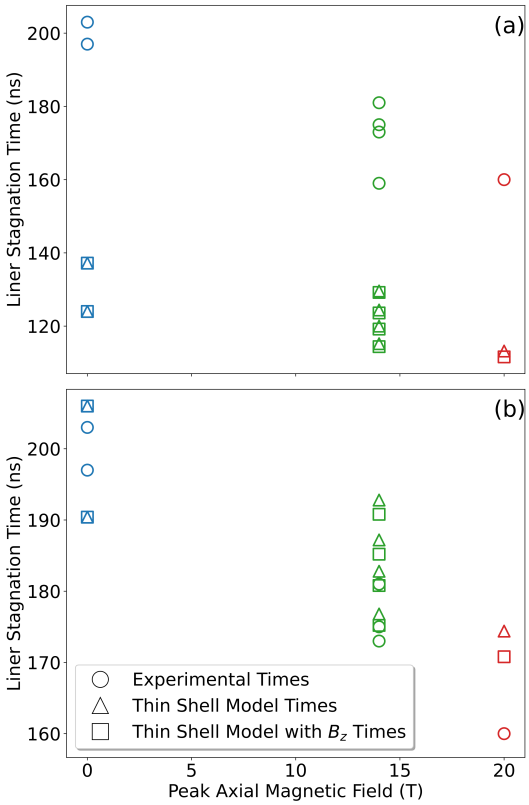

FIG. 12. Experimentally measured stagnation times, along with the stagnation times predicted from simple thin-shell implosion modeling. The thin-shell modeling was conducted in two ways: (1) considering only the drive pressure due to $B_\theta(t)$ (triangles), and (2) considering the drive pressure due to both B_θ and B_z (squares). Note that the low-field DSP case has been excluded from these plots since the additional drive pressure due to B_z is so small. (a) 100% of the measured load current is applied to the liner's outer surface. (b) 78% of the measured load current is allowed to run within the interior volume of the imploding liner, at a radius $r < r_\ell(t)$. This interior current generates magnetic pressure that opposes the implosion, thus increasing the stagnation times. The tuned fraction of 78% was chosen so that the modeled stagnation times matched the experimentally measured stagnation times in the SZP case. This same fraction was then applied to the DSP cases to observe the effects of adding B_z. Note the rescaling of the y-axis from (a) to (b).

indication that a significant fraction of the current delivered to the liner is flowing somewhere within the interior volume of the liner, at a radius $r < r_\ell(t)$. For example, interior currents could potentially flow along the surface of the on-axis support rod or somewhere within the low-density precursor plasma that is assumed to be streaming inward from the bulk liner material towards the on-axis support rod. Based on the flux compression measurements presented in Sec. III A, surface flashover of the on-axis support rod seems unlikely, because if the surface flashed over, then the measured $B_z(t)$ signal would have been excluded from the rod's interior, which is where the B-dot probe was housed. Therefore, it may be that much of the current was distributed at $r < r_\ell(t)$ in the rapidly advecting precursor plasma. Nevertheless, an interior current generates a magnetic pressure that opposes the liner implosion, thus increasing the stagnation time.

In Fig. 12(b), we present the effects of interior currents on the modeled stagnation times. These results were generated by adding an interior magnetic pressure source to our thin-shell model and repeating the analysis presented in Fig. 12(a). To generate Fig. 12(b), the fraction of the total measured load current that runs in the liner's interior volume was tuned so that the modeled stagnation time matched the experimentally measured stagnation times of the SZP case. This same fraction was then applied to the DSP cases to observe the effects of adding B_z. In doing this, we see better agreement with the experimental measurements. However, this method raises many questions, because to get this agreement, the interior current had to be set to 78% of the total measured current. Additionally, we are not able to fully account for the earlier stagnation times in the DSP cases, even when including the additional drive pressure supplied by B_z.

To help resolve these discrepancies in the future, more shots would be useful for improving the statistics. Additionally, axial imaging diagnostics and more detailed multi-physics MHD modeling would be useful to better understand how current and low-density plasmas are flowing in these thin-foil systems with on-axis support rods. Also, a more aggressive DSP design, one with a significantly higher G_0 value than the ones tested in these experiments (see Table I), would be helpful in trying to maximize the separation in stagnation times. Finally, to test coupling effects more directly, future experiments should be conducted using SZP/DSP cases that all use the same return-current radius and height. The subtle reasons for why this is important is discussed in detail in Appendix A.

D. Charged-particle dynamics in the power feed

An observation relevant to power flow dynamics was revealed by the drive-current waveforms presented in Fig. 5 of Ref. 41. For a given SZP/DSP configuration, the current waveforms were very reproducible. However, for the SZP case, the Rogowski coil appears to have shorted out (or become shielded by plasma) around 300 ns (as indicated by these time-integrated signals not returning to zero). By contrast, in most of the DSP experiments, the Rogowski coil continued to measure the drive current for the duration of the pulse.

One explanation of this behavior[69–72] is that, in the anode-cathode (A-K) gap, both the power flow and plasma flow reverse directions with voltage reversal, which occurs after peak current in these pulsed inductive systems, since $V \approx L\dot{I}$. This is illustrated for the SZP configuration in Fig. 13. Before and after peak current, the magnetic field $\mathbf{B}$ is in the same azimuthal direction,

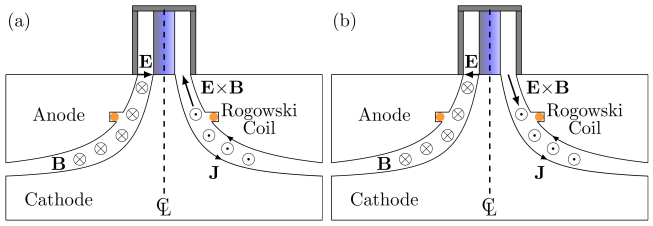

FIG. 13. Illustrations of the power feed in the SZP case with the direction of $\mathbf{E}\times\mathbf{B}$ (the Poynting vector) indicated at two times during the current pulse. (a) During the current rise, near the top of the swooping power feed, the electric field points radially inward, thus $\mathbf{E}\times\mathbf{B}$ points upward at this location. (b) During the falling edge of the current pulse (after peak current), the electric field vector has flipped directions, thus $\mathbf{E}\times\mathbf{B}$ points down the power feed, towards the Rogowski coil.

since the current continues running in the same direction. However, the direction of the electric field $\mathbf{E}$ changes sign after peak current, since $E \approx V/d \approx L\dot{I}/d$, where d is the A-K gap spacing. Thus, both the electromagnetic energy flux (i.e., the Poynting vector $\mathbf{S} = \mathbf{E}\times\mathbf{B}/\mu_0$) and the charged particle drift velocity ($\mathbf{v}_{\rm drift} = \mathbf{E}\times\mathbf{B}/B^2$) reverse directions after peak current—from radially inward and axially upward (towards the liner) to radially outward and axially downward (away from the liner and back towards the Rogowski coil, which is located in the power feed a few cm away from the liner).

The system power reversal can also lead to material ejection from electrode surfaces (including the liner's outer surface) into the A-K gap due to the inverse skin effect.[69,70] Before peak current, the magnetic field and the magnetic field pressure $p_{\rm mag} = B^2/(2\mu_0)$ continuously increase on the vacuum side of vacuum-electrode interfaces. This drives material into the electrodes, while the field and pressure also continuously diffuse into the electrode material. After peak current, the magnetic field at the vacuum-electrode interfaces can decrease faster than the magnetic field trapped inside the electrode bulk, because it takes time for the decreasing vacuum magnetic field to diffuse into the electrodes. Thus, the magnetic pressure in the A-K gap can become lower than the magnetic pressure trapped inside the electrode bulk. This can cause the outer layers of the electrode material (near the electrode surfaces) to explode outwards, into the A-K gap. Since $p_{\rm mag} = B^2/(2\mu_0) \propto I^2/r^2$ [with $B = \mu_0 I/(2\pi r)$], the largest variations in magnetic pressure will occur at the smallest radii in the system [e.g., $r_\ell(t)$], where the most intense ohmic heating can also take place, due to the large current densities at small radii. Therefore, the inverse skin effect can source low-density plasma into the A-K gap, which begins predominantly near the liner and then propagates radially outwards and axially downwards, towards the Rogowski coil, at the charged particle drift velocity $\mathbf{v}_{\rm drift} = \mathbf{E}\times\mathbf{B}/B^2$. Note that the drift velocity is the same for any charged particles (e.g., electrons and ions), as long as the particles are magnetized (i.e., as long as the their gyro radii are less than the A-K gap spacing, d).

It is possible that the bulk low-density plasma flow in the A-K gap could interfere with magnetic probe measurements, as observed in Ref. 71. This might then also explain the current waveforms observed for the SZP configuration in Fig. 5 of Ref. 41. Additionally, this may indicate that the DSP configuration somehow prevents low-density liner plasma from moving into the power feed towards the Rogowski coil, since the Rogowski coil was able to measure the drive current for the duration of the current pulse in the DSP-driven experiments of Fig. 5 in Ref. 41.

To further study this phenomenon, and to check how accurate our simple picture of the power feed is, 3D particle-in-cell (PIC) simulations were performed using CST EM studio software.[58] A geometrically simple power feed was constructed in the simulation using the A-K gap spacings of the COBRA power feed ($d \approx 1$ cm). From the bottom of the power feed (see Fig. 14), the simulation drives a prescribed current pulse with a 1-MA peak and a 100-ns rise time through the system. Current and voltage monitors were placed throughout the power feed to monitor the drive conditions. Open boundary conditions were used at five of the six simulation boundaries. The boundary where the bottom of the power feed sits is held at ground potential. Charged particles (electrons) were initialized with a Maxwellian distribution centered at 10 eV, in a cylindrical shell around the liner, since most of the plasma in our experiments was sourced from the ablated thin-foil liner. Electrons were added to the simulation in bunches of a thousand every 10 ns, starting at 70 ns, and stopping at 170 ns. Space-charge effects were included in the simulation but had a negligible effect due to the small number of particles.

The simulation results for the SZP case are presented in Fig. 14(a). Prior to peak current, the electrons bunch together and are well confined in the liner region. After peak current (e.g., at 160 ns), the electron bunch begins to drift towards the power feed. Eventually, all of the electrons pour down into the power feed, as described by our simple picture above.

The simulation results for the mid-field DSP case are presented in Fig. 14(b). Interestingly, regardless of the simulation time, due to the different magnetic topology of the DSP, electrons are continuously ejected radially outward through the gaps in the twisted return-current posts. Very few particles make their way into the power feed, even after peak current. Additionally, relative to the SZP case, the acceleration of the electrons to higher energies in the DSP simulation might be related to the brighter visible self-emission observed in the DSP images of Fig. 5.

The simulations presented for the SZP case in Fig. 14(a) do not prove that the Rogowski coil in our experiments would be affected by the electrons in the power feed, since the electrons in the simulation remain close to the cathode, while the Rogowski coil on CO-

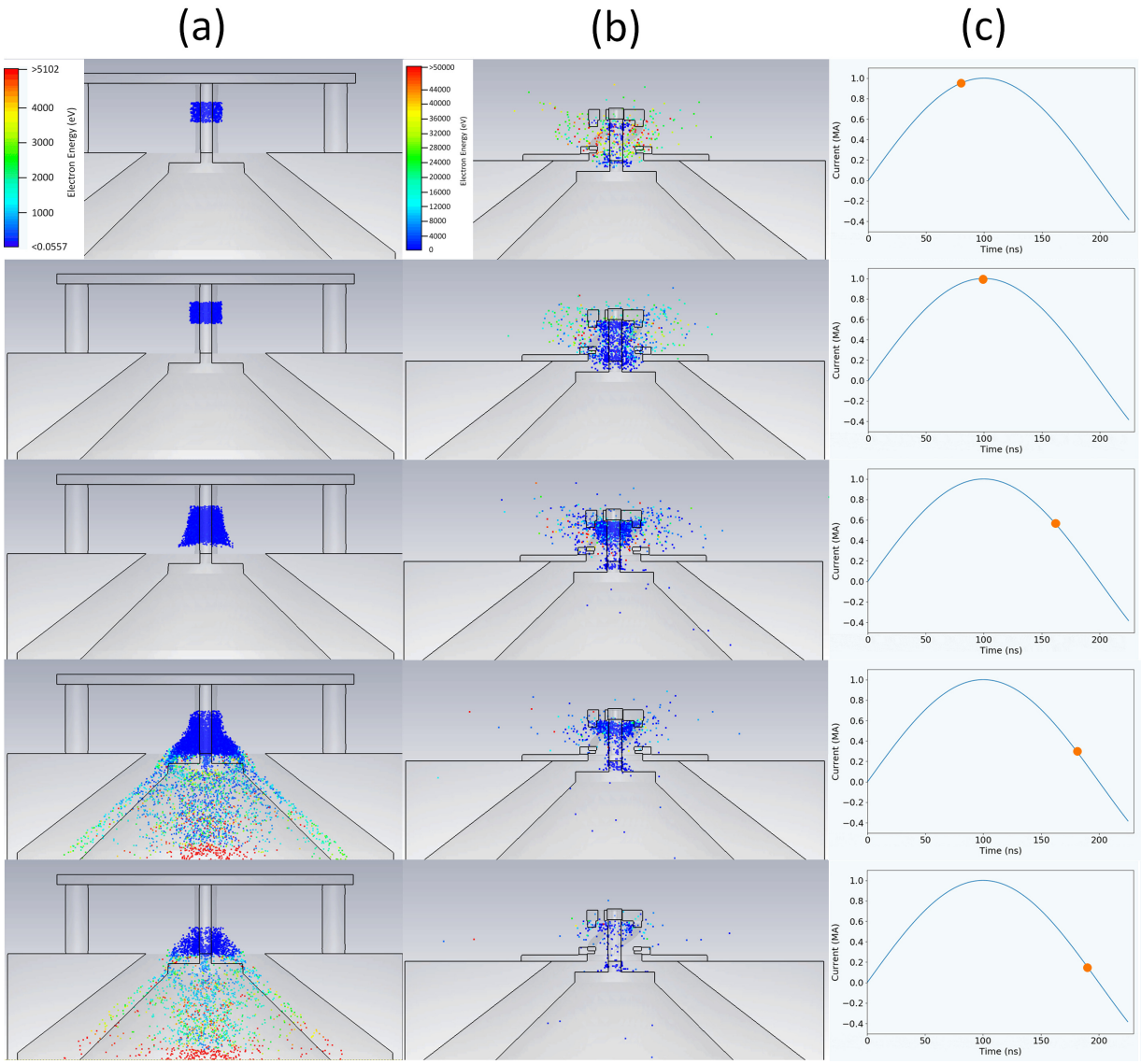

FIG. 14. Screenshots from 3D particle-in-cell simulations of electrons in the load region and power feed of (a) the SZP configuration with discrete straight return-current posts modeled and (b) the DSP configuration with discrete twisted return-current posts modeled. The screenshot times are indicated by the orange dot superimposed on the corresponding plot of the simulation's driving current pulse in column (c). The electrons were initialized with a Maxwellian energy distribution centered at 10 eV, in a cylindrical shell around the liner. In case (a), during the current rise, the electrons are well confined to their initial positions near the liner, but after voltage reversal, they are driven down into the power feed, where the Rogowski coil would be located in a COBRA experiment. In case (b), during both the current rise and fall, the electrons are continuously ejected out of the load region, through the gaps in the return current structure. Very few electrons make their way into the power feed, where the Rogowski coil would be located in a COBRA experiment.

BRA is embedded in a notch along the surface of the anode (see Fig. 13). However, we note that these preliminary simulations only included a few thousand electrons at any given moment, whereas in the experiments, there should be many orders of magnitude more particles (including magnetized hydrogen ions from desorbed surface contaminants) that could potentially fill the AK gap and interfere with the Rogowski coil. Furthermore, in Ref. 71, the use of two probe locations in MITLs provided experimental data that are consistent with low-density plasma moving away from the liner (after peak current) at a velocity of $\mathbf{v}_{\text{drift}} = \mathbf{E} \times \mathbf{B}/B^2$. In these experiments, the probe signals flatlined after peak current at times that were roughly proportional to the probe's distance from the liner.

The simulations presented for the DSP case in Fig. 14(b) show that charged particles created in the load region of the DSP configuration are not likely to

find their way into the power feed. Thus, these particles are not likely to interfere with the Rogowski coil, which may explain why the Rogowski coil was able to measure the drive current for the duration of the current pulse in the DSP-driven experiments of Fig. 5 in Ref. 41.

IV. SUMMARY, CONCLUSIONS, AND FUTURE WORK

The experimental results presented in this paper and in Ref. 41 have demonstrated enhanced stability in DSP-driven thin-foil liner implosions relative to comparable SZP-driven thin-foil liner implosions. At a convergence ratio of 2 ($C_r = 2$, $\hat{d} = 0.5$), the MRTI amplitudes for the SZP case and for the 14-T and 20-T DSP cases were, respectively, 1.1±0.3 mm, 0.7±0.2 mm, and 0.3±0.1 mm. While the maximum convergence ratio in these experiments was low (e.g., the MagLIF program is interested in maintaining stability up to $C_r \approx 4$–10 for the liner's outer surface), the trends in the data are clear—when the DSP generates stronger axial magnetic fields, the instability amplitudes decrease. This trend should continue in cases where the liner implodes past a convergence ratio of 2, where the stabilizing effects of the DSP should be further amplified.

The degree of relative stabilization measured from one SZP/DSP case to the next agrees reasonably well with that calculated using the analytic models of Velikovich and Schmit.[51] However, questions remain, as some of the input parameters to the analytic models are not sufficiently constrained by the experimental measurements—e.g., shell thickness, perturbation wavelength evolution, and $\phi_B(t)$. Such measurements could be made in the future via penetrating radiograph and polarization Zeeman spectroscopy. Furthermore, 3D MHD simulations are needed to better understand the nonlinear development of the helical instability structures, including the cascade from shorter to longer dominant wavelength structures.

Micro B-dot probe measurements showed that the return-current structures in the DSP cases generated axial magnetic fields in line with those predicted by electromagnetic simulations in CST. Measurements taken inside the imploding liners showed a significant amount of flux injection and compression. A flux conserving model was used to infer the position of the liner's inner surface, $r_{\text{in}}(t)$. The results showed that the measured $B_z(t)$ signals could have indeed been generated by flux injection and compression. In the future, more detailed modeling and simulation, as well as further experimentation, are needed to fully understand these measurements. For example, direct measurements of pre-filling "precursor" plasmas as well as the in-flight wall thickness of the imploding liner shell, perhaps via end-on laser probing and/or penetrating radiography, would be extremely valuable. A penetrating radiography capability would also enable MRTI feedthrough measurements.

Simple thin-shell modeling was not able to account for the much earlier stagnation times observed in the mid-field and high-field DSP cases (relative to the SZP case), even when adding the additional pressure due to B_z. Additionally, up to 78% of the measured load current may be flowing within ablated precursor plasma at $r < r_\ell(t)$, leading to delayed stagnation times across all of the SZP/DSP cases tested. More experiments are needed to resolve these discrepancies.

Preliminary PIC simulations of the mid-field DSP configuration found that electrons are continuously ejected radially outward through the gaps in the return-current structure, with very few electrons making their way into the power feed. By contrast, PIC simulations of the SZP case confirmed that electrons are driven into the power feed after peak current. This supports the idea that, in the SZP case, low-density plasma sourced near the liner can move out into the power feed after peak current, shield the Rogowski coil, and cause the flatlined SZP signals shown in Fig. 5 of Ref. 41. This flatlining is absent in the DSP waveforms of Fig. 5 in Ref. 41, which is consistent with very few electrons making their way into the power feed in the PIC simulations of the DSP case. In the future, these simulation efforts could be improved by including magnetized hydrogen ions as well as plasma sourcing from the electrode surfaces.

Our experiments on COBRA have demonstrated that the DSP configuration is an effective concept for liner stabilization. While MagLIF was the motivation behind the development of this concept,[39] other liner implosion experiments needing more stable interfaces could also benefit—e.g., cylindrical liner implosions for studies of material properties and equation of state.[4] Additionally, the power flow and magnetic flux compression results might be of interest to both fusion and non-fusion-related z-pinch research. The effects that the DSP has on liner implosions are profound. Hopefully, this work will serve as a foundation for further exploration into the various uses of the DSP.

ACKNOWLEDGMENTS

The authors would like to thank Sophia Rocco, Jacob Banasek, Harry Wilhelm, Todd Blanchard, and Daniel Hawkes for their assistance with these experiments, and Kyle Cochrane for his assistance with the LMD ECON table. This work was supported by the National Science Foundation under Grant No. PHY-1705418 of the NSF-DOE Partnership in Basic Plasma Science and Engineering. Facility support for COBRA was provided by the NNSA Stewardship Sciences Academic Programs under DOE Cooperative Agreement DE-NA0003764. Sandia National Laboratories is a multi-mission laboratory managed and operated by National Technology and Engineering Solutions of Sandia, LLC., a wholly owned subsidiary of Honeywell International, Inc., for the U.S. Department of Energy's National Nuclear Security Administration under contract DE-NA-0003525. The data that support the findings of this study are available from the

corresponding author upon reasonable request.

Appendix A: Flux concentration in a DSP

In this Appendix, we compare a DSP configuration with a SZP configuration, where both configurations have the same return-current radius and height, and thus the DSP configuration has a higher inductance. We do this to show that the DSP can still produce more magnetic drive pressure than its SZP counterpart, even though the DSP inductance is larger, and thus the total generator current in the DSP case is smaller.

In the DSP configuration with a perfectly conducting liner, the current density along the liner's outer surface follows a helical path, whereas in the SZP configuration, the current density follows a purely axial path. Initially, one might suspect that this simple change in direction should not result in a net increase in drive pressure. That is, when comparing a DSP configuration with a SZP configuration, where the same driver, the same power feed, the same liner, and the same return-current radius and height are used, the larger inductance of the DSP configuration means that, in the DSP case, the generator's $I(t)$ is lower, and thus J_z and B_θ are lower along the liner's outer surface. Therefore, one might suspect that, in the DSP case, the lower $B_\theta^2/(2\mu_0)$ pressure exactly cancels the added $B_z^2/(2\mu_0)$ pressure. However, exact cancellation does not occur. Whether the result is a net increase or decrease in total drive pressure depends on the specifics of the DSP design in relation to the driver characteristics, as described below.

To aid this discussion, we refer to Fig. 15, which shows the inner cylindrical conductor of a coaxial system delivering a pulsed surface current to a region with helical current flow (the region with helical current flow would be the liner in our DSP experiments). In this picture, both a streamline and vector representation of the current density driven along the outer surface of the inner conductor are shown. The total current supplied by (and returned to) the generator is $I = J_z \cdot 2\pi r$, where J_z is the axial component of the surface current density (in units of A/m). In the section with helical current flow, an azimuthal surface current density, J_θ, is induced along the liner's outer surface. The induction comes from the changing axial magnetic field, $\dot{B}_z$, generated by the surrounding helical return-current structure (not shown in Fig. 15). Note that J_θ must be induced on the liner's outer surface to satisfy the boundary condition for a pulsed magnetic field in vacuum adjacent to a perfect conductor: $B_z = \mu_0 J_\theta$. This means that J_θ does not originate from or return to the generator; it simply runs around the liner in the azimuthal direction, thus forming a separate circuit (or current loop) from the circuit (or current loop) that includes the generator.

Referring to Fig. 15(b), note that J_z in the helical section is equal to J_z in the pure axial sections above and below the helical section. This must be the case in order

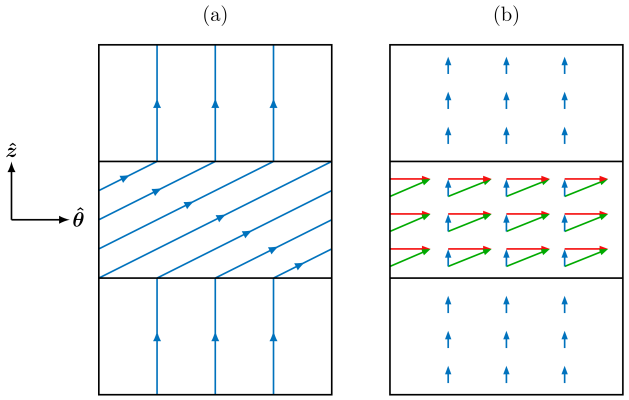

FIG. 15. Representations of the pulsed surface current density $\mathbf{J}$ along the outer surface of a cylindrical conductor, unwrapped in the $\hat{\boldsymbol{\theta}}$ direction. The central region, which represents the outer surface of a DSP-driven liner, has an induced J_θ, which results in a net helical current flow. (a) Streamlines of current, where the density of the streamlines indicates the magnitude $|\mathbf{J}|$. Geometrically, since every streamline of $\mathbf{J}$ flowing into the bottom of the helical section must flow out the top of the helical section, and since $\mathbf{J}$ becomes tilted in the helical section, the streamline density must increase in the helical section. Thus $|\mathbf{J}|$ must increase in the helical section. (b) A vector-arrow representation of $\mathbf{J}$, which shows that J_z (blue arrows) is continuous everywhere along this conductor, including across the interfaces between regions with helical and purely axial flows. Were this not the case, a local charge density $\rho(t)$ would build up at the interfaces between the regions.

to satisfy the charge continuity equation:

$$\nabla \cdot \mathbf{J} = \frac{1}{r}\frac{\partial}{\partial r}(rJ_r) + \frac{1}{r}\frac{\partial J_\theta}{\partial \theta} + \frac{\partial J_z}{\partial z} = -\frac{\partial \rho}{\partial t} = 0. \quad \text{(A1)}$$

Since J_θ is not varying in the $\hat{\boldsymbol{\theta}}$ direction, we know that $\frac{\partial J_\theta}{\partial \theta} = 0$, and because $J_r = 0$ everywhere, we know that $\frac{\partial}{\partial r}(rJ_r) = 0$. This leaves us with $\frac{\partial J_z}{\partial z} = -\frac{\partial \rho}{\partial t} = 0$. This tells us that J_z must be continuous everywhere along the cylinder's surface, including across the interfaces between the helical section and the pure axial sections, or else there would be an accumulation of charge over time at these interfaces.

The continuity of J_z means that the axial current I_z in the helical section is equal to the axial current in the sections above and below the helical section. Thus, I_z in the helical section is equal to the total current supplied by the generator. Superimposed on I_z in the helical section is an additional azimuthal current I_θ that is induced along the liner's outer surface. This current is equal in magnitude, but runs opposite to the azimuthal current running in the helical return-current structure. The additional azimuthal current along the liner's outer surface is consistent with the additional magnetic pressure due to the axial magnetic field, B_z, which causes the liner to implode earlier in the DSP case (relative to

the SZP case). This additional azimuthal current should not cause any alarm, however, as a similar phenomenon happens in transformers—i.e., the induced current in a secondary winding can exceed the generator current in the primary winding if an appropriate turns ratio and load impedance are used.

The increased current density along the liner's outer surface, $J = \sqrt{J_z^2 + J_\theta^2}$, can also be seen geometrically using Fig. 15(a). Note that this is equivalent to an increased $B = \sqrt{B_z^2 + B_\theta^2}$ and an increased $p_{\rm mag} = B^2/(2\mu_0) = (B_\theta^2 + B_z^2)/(2\mu_0)$ at the liner's outer surface due to the boundary conditions for a pulsed magnetic field in vacuum adjacent to a perfect conductor: $B_z = \mu_0 J_\theta$ and $B_\theta = \mu_0 J_z$. Due to the fact that every streamline of $\mathbf{J}$ flowing into the bottom of the helical section must flow out the top of the helical section, and that $\mathbf{J}$ becomes tilted in the helical section, the streamline density must therefore increase in the helical section. And since the density of streamlines represents the magnitude of $\mathbf{J}$ ($|\mathbf{J}| = J$), we know that J must be larger in the helical section (along the liner's outer surface) than in the axial sections above and below the helical section. The boundary condition for a pulsed magnetic field in vacuum adjacent to a perfect conductor holds in terms of absolute magnitudes as well—i.e., $B = \mu_0 J$, where the directions of $\mathbf{B}$ and $\mathbf{J}$ are perpendicular to one another, but both $\mathbf{B}$ and $\mathbf{J}$ follow helical paths along the liner's outer surface. This is the same thing as saying that the $\mathbf{J} \times \mathbf{B}$ force density is directly radially inwards everywhere, but in the SZP case, there is only one component $|J_z B_\theta|(-\hat{\boldsymbol{r}})$, while in the DSP case, there are two components $|J_z B_\theta|(-\hat{\boldsymbol{r}})$ and $|J_\theta B_z|(-\hat{\boldsymbol{r}})$, where the $J_\theta B_z$ component is an additional inward force density due to the θ-pinch effect.

Regardless of the higher current density, and thus the higher magnetic pressure in the helical section, the total energy in the system must always be conserved. All of the energy for the additional azimuthal current and axial magnetic field in the helical section must come from the pulsed-power generator. What is special about the DSP is that it allows us to concentrate the delivery of magnetic energy to the region where we want it (i.e., to the helical section with the imploding liner). To conserve total driver energy, the increased magnetic energy in the load region is balanced by having less magnetic energy present in the magnetically insulated transmission lines (MITLs). Building up excess magnetic energy in the MITLs is not useful for driving the implosion, since the liner is not located in the MITLs. Thus, the ability of the DSP configuration to change the distribution of magnetic energy from the MITL region to the load region is a distinct advantage of using the DSP configuration.

The redistribution of magnetic energy from the MITL region to the load region occurs in a DSP as follows. The pulsed-power generator applies a voltage V to the inductance of the entire vacuum cavity $L = L_{\rm load} + L_{\rm MITL}$. For simplicity, we will consider a static (non-imploding) liner. The applied voltage causes a current pulse to begin rising at a rate of $\dot{I} = V/L$, which is just Faraday's law for describing the rate of increasing magnetic flux in each vacuum region due to the applied voltage, or $V = L\dot{I} = \dot{\Phi} = \dot{\Phi}_{\rm load} + \dot{\Phi}_{\rm MITL}$. Note that $\dot{\Phi}$ is directly related to $\dot{I}$ and that we are applying a minus sign to Faraday's law to simplify the discussion—i.e., a positive voltage drives a positive increase in current and a positive increase in magnetic flux. The smaller $\dot{I}$ in the DSP case (due to the larger $L_{\rm load}$ and thus the larger $L = L_{\rm load} + L_{\rm MITL}$) means that $\dot{\Phi}_{\rm MITL}$ will be smaller in the DSP case, and thus $\dot{\Phi}_{\rm load}$ will be larger in the DSP case, since more of the generator's total $V = \dot{\Phi}_{\rm load} + \dot{\Phi}_{\rm MITL}$ is applied to the load. This means that in this particular case, where the DSP return-current radius is equal to the SZP return-current radius, more magnetic energy is delivered to the load region of the DSP case. Also note that in the DSP case, the total $\dot{\Phi}_{\rm load}$ has both azimuthal and axial components ($\dot{\Phi}_{{\rm load},\theta}$ and $\dot{\Phi}_{{\rm load},z}$) due to $\dot{B}_\theta$ and $\dot{B}_z$.

Since the volume of the DSP and SZP load regions are the same in this case (since we are assuming the same return-current radius and height), and since the DSP delivers more of the available driver energy to the load region, the spatially-averaged magnetic pressure $\langle p_{\rm mag}\rangle = \langle B^2\rangle/(2\mu_0)$ in the load region must be higher in the DSP case. However, for comparing drive pressures, we must evaluate and compare the local drive pressure $p_{\rm mag}(r)$ at the liner's outer surface, $r = r_\ell$. To do this, we recall that the pressure associated with $B_\theta(r)$ is preferentially distributed near the liner's outer surface, since $B_\theta(r) = \mu_0 I/(2\pi r) \propto 1/r$, while the pressure associated with $B_z = \mu_0 I n_c$ is distributed uniformly. Whether the total drive pressure is higher or lower for a particular DSP configuration, relative to the corresponding SZP configuration (where both configurations use the same return-current radius and height), comes down to the specifics of the configuration—e.g., the ratio of the return-current radius to the liner radius, the strength (or helicity) of the DSP return-current structure (i.e., the number of turns per unit length, n_c), and the ratio of $L_{\rm load}/L_{\rm MITL}$. These comparisons become quite complicated, particularly during the liner implosion, when the ratio of the return-current radius to the liner radius changes continuously.

To our knowledge, there is presently no convenient analytical way of expressing where the transition occurs for a DSP configuration to have a higher or lower drive pressure relative to a SZP configuration with the same return-current radius and height. Nevertheless, relative to a given SZP configuration, there are DSP configurations where the liner implodes and stagnates earlier in the DSP case, even when the same return-current radius and height are used in both configurations. We have investigated this numerically. Generally, the DSP provides higher drive pressure gains when the liner radius is closer to the return-current radius. As the liner implodes, the ratio of the liner radius to the return-current radius can become small enough that the DSP configuration begins

to generate less drive pressure relative to the SZP configuration; however, with proper design, by the time this transition occurs, the liner implosion can be effectively ballistic, and thus the overall time to stagnation can still be smaller in the DSP case.

Some of the cases evaluated numerically include a MITL inductance of ~ 10 nH, a liner radius of 3–4 mm, a return-current radius of 6–8 mm, a liner height of 10 mm, and (for the DSP configuration) an initial B_z/B_θ ratio of 0.5–1.0. These cases give load inductance values of approximately 2–8 nH and initial drive pressure ratios $p_{\mathrm{mag,DSP}}/p_{\mathrm{mag,SZP}}$ of 1.05–1.2. Integrating the DSP's higher initial drive pressure over time results in the DSP's implosion starting earlier than the SZP's implosion. Later in time, as the liner moves to smaller radii, the ratio $p_{\mathrm{mag,DSP}}/p_{\mathrm{mag,SZP}}$ can drop to ~ 0.7–0.9. Nevertheless, the momentum imparted early in time can cause the overall time to stagnation to be shorter in the DSP case.

We stress here that the same return-current radius was not used in the SZP and DSP cases tested on COBRA. In our COBRA experiments, the return-current radii selected for the DSP cases were smaller than the return-current radius used for the SZP case. This was done to equalize L_{load} between the cases. With approximately equal values for L_{load}, the total current I delivered from the generator to the load is approximately the same in all the cases. This means that I_z is approximately the same in all cases. However, the DSP cases have an additional I_θ, which is consistent with an additional J_θ and B_z. Thus, we have $p_{\mathrm{mag,DSP}} = (B_\theta^2+B_z^2)/(2\mu_0) > p_{\mathrm{mag,SZP}} = B_\theta^2/(2\mu_0)$. This means that in our experiments, the DSP cases should always implode earlier.

To more directly test the potential benefits of the improved coupling efficiency in the DSP configuration, future experiments should compare SZP and DSP configurations where the load volume is kept constant across all cases tested—i.e., the same load heights, liner dimensions, and return-current radii should be used in all cases. With carefully designed experiments, certain DSP configurations should reduce the generator current while still resulting in earlier implosion times.

[1] D. D. Ryutov, M. S. Derzon, and M. K. Matzen, "The physics of fast Z pinches," Rev. Mod. Phys. **72**, 167–223 (2000).

[2] M. G. Haines, "A review of the dense Z-pinch," Plasma Physics and Controlled Fusion **53**, 093001 (2011).

[3] M. R. Martin, R. W. Lemke, R. D. McBride, J. P. Davis, D. H. Dolan, M. D. Knudson, K. R. Cochrane, D. B. Sinars, I. C. Smith, M. Savage, W. A. Stygar, K. Killebrew, D. G. Flicker, and M. C. Herrmann, "Solid liner implosions on Z for producing multi-megabar, shockless compressions," Phys. Plasmas **19**, 056310 (2012).

[4] R. W. Lemke, D. H. Dolan, D. G. Dalton, J. L. Brown, K. Tomlinson, G. R. Robertson, M. D. Knudson, E. Harding, A. E. Mattsson, J. H. Carpenter, R. R. Drake, K. Cochrane, B. E. Blue, A. C. Robinson, and T. R. Mattsson, "Probing off-Hugoniot states in Ta, Cu, and Al to 1000 GPa compression with magnetically driven liner implosions," J. Appl. Phys. **119**, 015904 (2016).

[5] G. A. Rochau, J. E. Bailey, R. E. Falcon, G. P. Loisel, T. Nagayama, R. C. Mancini, I. Hall, D. E. Winget, M. H. Montgomery, and D. A. Liedahl, "ZAPP: The Z Astrophysical Plasma Properties collaboration," Phys. Plasmas **21**, 056308 (2014).

[6] J. E. Bailey, T. Nagayama, G. P. Loisel, G. A. Rochau, C. Blancard, J. Colgan, P. Cosse, G. Faussurier, C. J. Fontes, F. Gilleron, I. Golovkin, S. B. Hansen, C. A. Iglesias, D. P. Kilcrease, J. J. MacFarlane, R. C. Mancini, S. N. Nahar, C. Orban, J.-C. Pain, A. K. Pradhan, M. Sherrill, and B. G. Wilson, "A higher-than-predicted measurement of iron opacity at solar interior temperatures," Nature **517**, 56–59 (2015).

[7] G. A. Rochau, J. E. Bailey, G. A. Chandler, G. Cooper, G. S. Dunham, P. W. Lake, R. J. Leeper, R. W. Lemke, T. A. Mehlhorn, A. Nikroo, K. J. Peterson, C. L. Ruiz, D. G. Schroen, S. A. Slutz, D. Steinman, W. A. Stygar, and W. Varnum, "High performance capsule implosions driven by the Z-pinch dynamic hohlraum," Plasma Physics and Controlled Fusion **49**, B591 (2007).

[8] D. J. Ampleford, B. Jones, C. A. Jennings, S. B. Hansen, M. E. Cuneo, A. J. Harvey-Thompson, G. A. Rochau, C. A. Coverdale, A. R. Laspe, T. M. Flanagan, N. W. Moore, D. B. Sinars, D. C. Lamppa, E. C. Harding, J. W. Thornhill, J. L. Giuliani, Y.-K. Chong, J. P. Apruzese, A. L. Velikovich, A. Dasgupta, N. Ouart, W. A. Sygar, M. E. Savage, J. K. Moore, R. Focia, T. C. Wagoner, K. L. Killebrew, A. D. Edens, G. S. Dunham, M. C. Jones, P. W. Lake, D. S. Nielsen, M. Wu, A. L. Carlson, M. D. Kernahan, C. R. Ball, R. D. Scharberg, T. D. Mulville, E. W. Breden, C. S. Speas, G. Olivas, M. A. Sullivan, A. J. York, D. W. Justus, J. C. Cisneros, T. Strizic, J. Reneker, M. Cleveland, M. P. Vigil, G. Robertson, D. Sandoval, C. Cox, A. J. Maurer, D. A. Graham, N. B. Huynh, S. Toledo, L. P. Molina, M. R. Lopez, F. W. Long, G. R. McKee, J. L. Porter, and M. C. Herrmann, "Contrasting physics in wire array z pinch sources of 1-20 keV emission on the Z facility," Physics of Plasmas **21**, 056708 (2014).

[9] S. A. Slutz, M. C. Herrmann, R. A. Vesey, A. B. Sefkow, D. B. Sinars, D. C. Rovang, K. J. Peterson, and M. E. Cuneo, "Pulsed-power-driven cylindrical liner implosions of laser preheated fuel magnetized with an axial field," Physics of Plasmas **17**, 056303 (2010).

[10] S. A. Slutz and R. A. Vesey, "High-Gain Magnetized Inertial Fusion," Phys. Rev. Lett. **108**, 025003 (2012).

[11] M. E. Cuneo, M. C. Herrmann, D. B. Sinars, S. A. Slutz, W. A. Stygar, R. A. Vesey, A. B. Sefkow, G. A. Rochau, G. A. Chandler, J. E. Bailey, J. L. Porter, R. D. McBride, D. C. Rovang, M. G. Mazarakis, E. P. Yu, D. C. Lamppa, K. J. Peterson, C. Nakhleh, S. B. Hansen, A. J. Lopez, M. E. Savage, C. A. Jennings, M. R. Martin, R. W. Lemke, B. W. Atherton, I. C. Smith, P. K. Rambo, M. Jones, M. R. Lopez, P. J. Christenson, M. A. Sweeney, B. Jones, L. A. McPherson, E. Harding, M. R. Gomez, P. F. Knapp, T. J. Awe, R. J. Leeper, C. L. Ruiz, G. W. Cooper, K. D. Hahn, J. McKenney, A. C. Owen, G. R. McKee, G. T. Leifeste, D. J. Ampleford, E. M. Waisman, A. Harvey-Thompson, R. J. Kaye, M. H. Hess, S. E. Rosenthal, and M. K. Matzen, "Magnetically Driven Implosions for Inertial Confinement Fusion at Sandia National Laboratories," IEEE Transactions on Plasma Science **40**, 3222–3245 (2012).

[12] M. R. Gomez, S. A. Slutz, A. B. Sefkow, D. B. Sinars, K. D. Hahn, S. B. Hansen, E. C. Harding, P. F. Knapp, P. F. Schmit, C. A. Jennings, T. J. Awe, M. Geissel, D. C. Rovang, G. A. Chandler, G. W. Cooper, M. E. Cuneo, A. J. Harvey-Thompson, M. C. Herrmann, M. H. Hess, O. Johns, D. C. Lamppa, M. R. Martin, R. D. McBride, K. J. Peterson, J. L. Porter, G. K. Robertson, G. A. Rochau, C. L. Ruiz, M. E. Savage, I. C. Smith, W. A. Stygar, and R. A. Vesey, "Experimental Demonstration of Fusion-Relevant Conditions in Magnetized Liner Inertial Fusion," Phys. Rev. Lett. **113**, 155003 (2014).

[13] M. R. Gomez, S. A. Slutz, C. A. Jennings, D. J. Ampleford, M. R. Weis, C. E. Myers, D. A. Yager-Elorriaga, K. D. Hahn, S. B. Hansen, E. C. Harding, A. J. Harvey-Thompson, D. C. Lamppa, M. Mangan, P. F. Knapp, T. J. Awe, G. A. Chandler, G. W. Cooper, J. R. Fein, M. Geissel, M. E. Glinsky, W. E. Lewis, C. L. Ruiz, D. E. Ruiz, M. E. Savage, P. F. Schmit, I. C.

Smith, J. D. Styron, J. L. Porter, B. Jones, T. R. Mattsson, K. J. Peterson, G. A. Rochau, and D. B. Sinars, "Performance scaling in magnetized liner inertial fusion experiments," Phys. Rev. Lett. **125**, 155002 (2020).

[14]E. G. Harris, "Rayleigh-Taylor Instabilities of a Collapsing Cylindrical Shell in a Magnetic Field," Phys. Fluids **5**, 1057–1062 (1962).

[15]E. Ott, "Nonlinear evolution of the Rayleigh-Taylor instability of a thin layer," Phys. Rev. Lett. **29**, 1429–1432 (1972).

[16]R. E. Reinovsky, W. E. Anderson, W. L. Atchison, C. E. Ekdahl, R. J. Faehl, I. R. Lindemuth, D. V. Morgan, M. Murillo, J. L. Stokes, and J. S. Shlachter, "Instability growth in magnetically imploded high-conductivity cylindrical liners with material strength," IEEE Trans. Plasma Sci. **30**, 1764 – 1776 (2002).

[17]A. R. Miles, "Nonlinear Rayleigh-Taylor instabilities in fast Z pinches," Phys. Plasmas **16**, 032702 (2009).

[18]D. B. Sinars, S. A. Slutz, M. C. Herrmann, R. D. McBride, M. E. Cuneo, K. J. Peterson, R. A. Vesey, C. Nakhleh, B. E. Blue, K. Killebrew, D. Schroen, K. Tomlinson, A. D. Edens, M. R. Lopez, I. C. Smith, J. Shores, V. Bigman, G. R. Bennett, B. W. Atherton, M. Savage, W. A. Stygar, G. T. Leifeste, and J. L. Porter, "Measurements of Magneto-Rayleigh-Taylor Instability Growth during the Implosion of Initially Solid Al Tubes Driven by the 20-MA, 100-ns Z Facility," Phys. Rev. Lett. **105**, 185001 (2010).

[19]Y. Y. Lau, J. C. Zier, I. M. Rittersdorf, M. R. Weis, and R. M. Gilgenbach, "Anisotropy and feedthrough in magneto-rayleigh-taylor instability," Phys. Rev. E **83**, 066405 (2011).

[20]P. Zhang, Y. Y. Lau, I. M. Rittersdorf, M. R. Weis, R. M. Gilgenbach, D. Chalenski, and S. A. Slutz, "Effects of magnetic shear on magneto-Rayleigh-Taylor instability," Physics of Plasmas **19**, 022703 (2012).

[21]M. R. Weis, P. Zhang, Y. Y. Lau, P. F. Schmit, K. J. Peterson, M. Hess, and R. M. Gilgenbach, "Coupling of sausage, kink, and magneto-Rayleigh-Taylor instabilities in a cylindrical liner," Physics of Plasmas **22**, 032706 (2015).

[22]A. B. Bud'ko, M. A. Liberman, A. L. Velikovich, and F. S. Felber, "Suppression of Rayleigh–Taylor and bulk convective instabilities in imploding plasma liners and pinches," Physics of Fluids B: Plasma Physics **2**, 1159–1169 (1990).

[23]F. L. Cochran and A. E. Robson, "Viscoresistive stabilization of the z pinch," Physics of Fluids B: Plasma Physics **5**, 2905–2908 (1993).

[24]A. B. Bud'ko, Y. P. Kravchenko, and M. A. Liberman, "Stabilization of sausage and kink instability modes of a plasma pinch by radial oscillations," Physics of Plasmas **2**, 792–802 (1995).

[25]U. Shumlak and C. W. Hartman, "Sheared flow stabilization of the $m = 1$ kink mode in Z pinches," Phys. Rev. Lett. **75**, 3285–3288 (1995).

[26]A. L. Velikovich and J. Davis, "Implosions, equilibria, and stability of rotating, radiating z-pinch plasmas," Physics of Plasmas **2**, 4513–4520 (1995).

[27]A. L. Velikovich, F. L. Cochran, J. Davis, and Y. K. Chong, "Stabilized radiative z-pinch loads with tailored density profiles," Physics of Plasmas **5**, 3377–3388 (1998).

[28]L. F. Wanex, V. I. Sotnikov, and J. N. Leboeuf, "Linear analysis of magnetic and flow shear stabilization of z-pinch instabilities," Physics of Plasmas **12**, 042101 (2005).

[29]K. J. Peterson, T. J. Awe, E. P. Yu, D. B. Sinars, E. S. Field, M. E. Cuneo, M. C. Herrmann, M. Savage, D. Schroen, K. Tomlinson, and C. Nakhleh, "Electrothermal Instability Mitigation by Using Thick Dielectric Coatings on Magnetically Imploded Conductors," Phys. Rev. Lett. **112**, 135002 (2014).

[30]T. J. Awe, K. J. Peterson, E. P. Yu, R. D. McBride, D. B. Sinars, M. R. Gomez, C. A. Jennings, M. R. Martin, S. E. Rosenthal, D. G. Schroen, A. B. Sefkow, S. A. Slutz, K. Tomlinson, and R. A. Vesey, "Experimental Demonstration of the Stabilizing Effect of Dielectric Coatings on Magnetically Accelerated Imploding Metallic Liners," Phys. Rev. Lett. **116**, 065001 (2016).

[31]J. D. Pecover and J. P. Chittenden, "Instability growth for magnetized liner inertial fusion seeded by electro-thermal, electrochoric, and material strength effects," Phys. Plasmas **22**, 102701 (2015).

[32]M. Evans, M. B. Adams, P. C. Campbell, N. M. Jordan, S. M. Miller, N. B. Ramey, R. V. Shapovalov, J. Young, I. West-Abdallah, J. M. Woolstrum, R. D. McBride, and P.-A. Gourdain, "Reduction of ablated surface expansion in pulsed-power-driven experiments using an aerosol dielectric coating," Physics of Plasmas **26**, 070704 (2019).

[33]A. M. Steiner, P. C. Campbell, D. A. Yager-Elorriaga, K. R. Cochrane, T. R. Mattsson, N. M. Jordan, R. D. McBride, Y. Y. Lau, and R. M. Gilgenbach, "The electro-thermal stability of tantalum relative to aluminum and titanium in cylindrical liner ablation experiments at 550 ka," Physics of Plasmas **25**, 032701 (2018).

[34]R. D. McBride, S. A. Slutz, C. A. Jennings, D. B. Sinars, M. E. Cuneo, M. C. Herrmann, R. W. Lemke, M. R. Martin, R. A. Vesey, K. J. Peterson, A. B. Sefkow, C. Nakhleh, B. E. Blue, K. Killebrew, D. Schroen, T. J. Rogers, A. Laspe, M. R. Lopez, I. C. Smith, B. W. Atherton, M. Savage, W. A. Stygar, and J. L. Porter, "Penetrating radiography of imploding and stagnating beryllium liners on the Z accelerator," Phys. Rev. Lett. **109**, 135004 (2012).

[35]R. D. McBride, M. R. Martin, R. W. Lemke, J. B. Greenly, C. A. Jennings, D. C. Rovang, D. B. Sinars, M. E. Cuneo, M. C. Herrmann, S. A. Slutz, C. W. Nakhleh, D. D. Ryutov, J.-P. Davis, D. G. Flicker, B. E. Blue, K. Tomlinson, D. Schroen, R. M. Stamm, G. E. Smith, J. K. Moore, T. J. Rogers, G. K. Robertson, R. J. Kamm, I. C. Smith, M. Savage, W. A. Stygar, G. A. Rochau, M. Jones, M. R. Lopez, J. L. Porter, and M. K. Matzen, "Beryllium liner implosion experiments on the z accelerator in preparation for magnetized liner inertial fusion," Physics of Plasmas **20**, 056309 (2013).

[36]S. A. Sorokin and S. A. Chaikovskii, Plasma Phys. Rep. **19**, 444 (1993).

[37]S. A. Sorokin and S. A. Chaikovsky, "Imploding Liner Stabilization Experiments on the SNOP-3 Generator," AIP Conf. Proc. **299**, 83–92 (1994).

[38]S. A. Sorokin, "Gas-puff liner implosion in the configuration with helical current return rods," Plasma Physics Reports **39**, 139–143 (2013).

[39]P. F. Schmit, A. L. Velikovich, R. D. McBride, and G. K. Robertson, "Controlling Rayleigh-Taylor Instabilities in Magnetically Driven Solid Metal Shells by Means of a Dynamic Screw Pinch," Phys. Rev. Lett. **117**, 205001 (2016).

[40]G. A. Shipley, C. A. Jennings, and P. F. Schmit, "Design of dynamic screw pinch experiments for magnetized liner inertial fusion," Physics of Plasmas **26**, 102702 (2019).

[41]P. C. Campbell, T. M. Jones, J. M. Woolstrum, N. M. Jordan, P. F. Schmit, J. B. Greenly, W. M. Potter, E. S. Lavine, B. R. Kusse, D. A. Hammer, and R. D. McBride, "Stabilization of Liner Implosions via a Dynamic Screw Pinch," Phys. Rev. Lett. **125**, 035001 (2020).

[42]D. C. Rovang, D. C. Lamppa, M. E. Cuneo, A. C. Owen, J. McKenney, D. W. Johnson, S. Radovich, R. J. Kaye, R. D. McBride, C. S. Alexander, T. J. Awe, S. A. Slutz, A. B. Sefkow, T. A. Haill, P. A. Jones, J. W. Argo, D. G. Dalton, G. K. Robertson, E. M. Waisman, D. B. Sinars, J. Meissner, M. Milhous, D. N. Nguyen, and C. H. Mielke, "Pulsed-coil magnet systems for applying uniform 10–30 T fields to centimeter-scale targets on Sandia's Z facility," Rev. Sci. Instrum. **85**, 124701 (2014).

[43]P. F. Schmit, P. F. Knapp, S. B. Hansen, M. R. Gomez, K. D. Hahn, D. B. Sinars, K. J. Peterson, S. A. Slutz, A. B. Sefkow, T. J. Awe, E. Harding, C. A. Jennings, G. A. Chandler, G. W. Cooper, M. E. Cuneo, M. Geissel, A. J. Harvey-Thompson, M. C. Herrmann, M. H. Hess, O. Johns, D. C. Lamppa, M. R. Martin, R. D. McBride, J. L. Porter, G. K. Robertson, G. A. Rochau, D. C. Rovang, C. L. Ruiz, M. E. Savage, I. C. Smith, W. A. Stygar, and R. A. Vesey, "Understanding Fuel Magnetization and Mix Using Secondary Nuclear Reactions in Magneto-Inertial Fu-

sion," Phys. Rev. Lett. **113**, 155004 (2014).
[44]P.-A. Gourdain, M. B. Adams, J. R. Davies, and C. E. Seyler, "Axial magnetic field injection in magnetized liner inertial fusion," Phys. Plasmas **24**, 102712 (2017).
[45]T. J. Awe, R. D. McBride, C. A. Jennings, D. C. Lamppa, M. R. Martin, D. C. Rovang, S. A. Slutz, M. E. Cuneo, A. C. Owen, D. B. Sinars, K. Tomlinson, M. R. Gomez, S. B. Hansen, M. C. Herrmann, J. L. McKenney, C. Nakhleh, G. K. Robertson, G. A. Rochau, M. E. Savage, D. G. Schroen, and W. A. Stygar, "Observations of Modified Three-Dimensional Instability Structure for Imploding z-Pinch Liners that are Premagnetized with an Axial Field," Phys. Rev. Lett. **111**, 235005 (2013).
[46]D. A. Yager-Elorriaga, Y. Y. Lau, P. Zhang, P. C. Campbell, A. M. Steiner, N. M. Jordan, R. D. McBride, and R. M. Gilgenbach, "Evolution of sausage and helical modes in magnetized thin-foil cylindrical liners driven by a Z-pinch," Physics of Plasmas **25**, 056307 (2018).
[47]D. D. Ryutov, T. J. Awe, S. B. Hansen, R. D. McBride, K. J. Peterson, D. B. Sinars, and S. A. Slutz, "Effect of axial magnetic flux compression on the magnetic Rayleigh-Taylor instability (theory)," AIP Conference Proceedings **1639**, 63–66 (2014).
[48]C. E. Seyler, M. R. Martin, and N. D. Hamlin, "Helical instability in MagLIF due to axial flux compression by low-density plasma," Phys. Plasmas **25**, 062711 (2018).
[49]J. M. Woolstrum, D. A. Yager-Elorriaga, P. C. Campbell, N. M. Jordan, C. E. Seyler, and R. D. McBride, "Extended magnetohydrodynamics simulations of thin-foil z-pinch implosions with comparison to experiments," Physics of Plasmas **27**, 092705 (2020).
[50]C. E. Seyler, "Axial magnetic flux amplification in Hall-magnetohydrodynamic simulations of externally magnetized z-pinches," Phys. Plasmas **27**, 092102 (2020).
[51]A. L. Velikovich and P. F. Schmit, "Bell-Plesset effects in Rayleigh-Taylor instability of finite-thickness spherical and cylindrical shells," Physics of Plasmas **22**, 122711 (2015).
[52]J. B. Greenly, J. D. Douglas, D. A. Hammer, B. R. Kusse, S. C. Glidden, and H. D. Sanders, "A 1ma, variable risetime pulse generator for high energy density plasma research," Review of Scientific Instruments **79**, 073501 (2008).
[53]T. A. Shelkovenko and D. A. Chalenski and K. M. Chandler and J. D. Douglass and J. B. Greenly and D. A. Hammer and B. R. Kusse and R. D. McBride and S. A. Pikuz, "Diagnostics on the cobra pulsed power generator," Review of Scientific Instruments **77**, 10F521 (2006).
[54]J. C. Zier, R. M. Gilgenbach, D. A. Chalenski, Y. Y. Lau, D. M. French, M. R. Gomez, S. G. Patel, I. M. Rittersdorf, A. M. Steiner, M. Weis, P. Zhang, M. Mazarakis, M. E. Cuneo, and M. Lopez, "Magneto-Rayleigh-Taylor experiments on a MegaAmpere linear transformer driver," Phys. Plasmas **19**, 032701 (2012).
[55]M. R. Weis, *Magneto-Rayleigh-Taylor Instability: Theory and Simulation in Planar and Cylindrical Pulsed Power Targets*, Ph.D. thesis, University of Michigan (2015).
[56]D. A. Yager-Elorriaga, P. Zhang, A. M. Steiner, N. M. Jordan, P. C. Campbell, Y. Y. Lau, and R. M. Gilgenbach, "Discrete helical modes in imploding and exploding cylindrical, magnetized liners," Phys. Plasmas **23**, 124502 (2016).
[57]D. A. Yager-Elorriaga, A. M. Steiner, S. G. Patel, N. M. Jordan, Y. Y. Lau, and R. M. Gilgenbach, "Technique for fabrication of ultrathin foils in cylindrical geometry for liner-plasma implosion experiments with sub-megaampere currents," Review of Scientific Instruments **86**, 113506 (2015).
[58]`https://www.cst.com/products/cstems`.
[59]J. Greenly, M. Martin, I. Blesener, D. Chalenski, P. Knapp, and R. McBride, "The Role of Flux Advection in the Development of the Ablation Streams and Precursors of Wire Array Z-pinches," AIP Conference Proceedings **1088**, 53–56 (2009).
[60]T. Byvank, *Applied Axial Magnetic Field Effects on Extended Magnetohydrodynamics Laboratory Plasma Jets: Experiments and Simulations*, Ph.D. thesis, Cornell University (2018).
[61]H. E. Knoepfel, *Magnetic Fields: A Comprehensive Theoretical Treatise for Practical Use* (John Wiley & Sons, Inc., 2000).
[62]S. P. Lyon and J. D. Johnson, "SESAME: The Los Alamos National Laboratory Equation of State Database," Technical Report No. LA-UR-92-3407, Los Alamos National Laboratory, Los Alamos, NM, 1992.
[63]M. Desjarlais, "Practical improvements to the lee-more conductivity near the metal-insulator transition," Contributions to Plasma Physics **41**, 267–270 (2001).
[64]M. P. Desjarlais, J. D. Kress, and L. A. Collins, "Electrical conductivity for warm, dense aluminum plasmas and liquids," Phys. Rev. E **66**, 025401 (2002).
[65]G. Burdiak, S. Lebedev, R. Drake, A. Harvey-Thompson, G. Swadling, F. Suzuki-Vidal, J. Skidmore, L. Suttle, E. Khoory, L. Pickworth, P. de Grouchy, G. Hall, S. Bland, M. Weinwurm, and J. Chittenden, "The production and evolution of multiple converging radiative shock waves in gas-filled cylindrical liner z-pinch experiments," High Energy Density Physics **9**, 52–62 (2013).
[66]L. Atoyan, D. A. Hammer, B. R. Kusse, T. Byvank, A. D. Cahill, J. B. Greenly, S. A. Pikuz, and T. A. Shelkovenko, "Helical plasma striations in liners in the presence of an external axial magnetic field," Physics of Plasmas **23**, 022708 (2016).
[67]M. M. Basko, "Rayleigh–Taylor eigenmodes of a thin layer in the nonlinear regime," Phys. Plasmas **1**, 1270–1278 (1994).
[68]D. D. Ryutov and M. A. Dorf, "Evolution of helical perturbations in a thin-shell model of an imploding liner," Physics of Plasmas **21**, 112704 (2014).
[69]M. G. Haines, "The Inverse Skin Effect," Proceedings of the Physical Society **74**, 576 (1959).
[70]J. Greenly, C. Seyler, and X. Zhao, "Pulsed-power driven reconnection and the inverse skin effect," Paper JP8 97, Bull. Am. Phys. Soc. **59**, 133 (2014).
[71]P. C. Campbell, J. M. Woolstrum, F. Antoulinakis, T. M. Jones, D. A. Yager-Elorriaga, S. M. Miller, N. M. Jordan, Y. Y. Lau, R. M. Gilgenbach, and R. D. Mcbride, "Diagnostic and power feed upgrades to the MAIZE facility," IEEE Transactions on Plasma Science **46**, 3973–3981 (2018).
[72]R. D. McBride, W. A. Stygar, M. E. Cuneo, D. B. Sinars, M. G. Mazarakis, J. J. Leckbee, M. E. Savage, B. T. Hutsel, J. D. Douglass, M. L. Kiefer, B. V. Oliver, G. R. Laity, M. R. Gomez, D. A. Yager-Elorriaga, S. G. Patel, B. M. Kovalchuk, A. A. Kim, P. . Gourdain, S. N. Bland, S. Portillo, S. C. Bott-Suzuki, F. N. Beg, Y. Maron, R. B. Spielman, D. V. Rose, D. R. Welch, J. C. Zier, J. W. Schumer, J. B. Greenly, A. M. Covington, A. M. Steiner, P. C. Campbell, S. M. Miller, J. M. Woolstrum, N. B. Ramey, A. P. Shah, B. J. Sporer, N. M. Jordan, Y. Y. Lau, and R. M. Gilgenbach, "A primer on pulsed power and linear transformer drivers for high energy density physics applications," IEEE Transactions on Plasma Science **46**, 3928–3967 (2018).